의학박사 학위논문

Characterization of Lymphatic Efflux of Cerebrospinal Space Fluid in Mouse Models by [^{64}Cu]Cu-Albumin Clearance Imaging

마우스 모델에서 [^{64}Cu]Cu-Albumin 분자영상을 활용한 뇌척수액의 림프 유출 규명

2022 年 **08** 月

서울대학교 의과대학

핵의학교실

Azmal Kabir Sarker

Doctoral Thesis

Characterization of Lymphatic Efflux of Cerebrospinal Space Fluid in Mouse Models by [^{64}Cu]Cu-Albumin Clearance Imaging

August 2022

Seoul National University College of Medicine

Nuclear Medicine

Azmal Kabir Sarker

마우스 모델에서 [^{64}Cu]Cu-Albumin 분자영상을 활용한 뇌척수액의 림프 유출 규명

지도교수 이동수

이 논문을 의학박사 학위논문으로 제출함

2022 年 **08** 月

서울대학교 의과대학

핵의학교실

Azmal Kabir Sarker

Azmal Kabir Sarker 의 의학박사 학위논문을 인준함

2022 年 **07** 月

위원장 _____

부위원장 _____

위원 _____

위원 _____

위원 _____

Abstract

Characterization of Lymphatic Efflux of Cerebrospinal Space Fluid in Mouse Models by [^{64}Cu]Cu-Albumin Clearance Imaging

Azmal Kabir Sarker

Department of Nuclear Medicine

Seoul National University College of Medicine

Purpose

The methodology for evaluation of clearance of brain waste in the cerebrospinal fluid (CSF) through the meningeal lymphatic vessels (MLV) has remained largely dependent upon fluorescent imaging and magnetic resonance imaging (MRI). These modalities have some inherent limitations in the context of animal physiology and sustainable clinical translatability. Therefore, the experiment was designed firstly to establish a molecular imaging protocol for the evaluation of lymphatic efflux of CSF in adult mice and then to apply the protocol on aged mice to explore age related variation in the lymphatic efflux of CSF.

Methods

Radionuclide imaging after intrathecal (IT) injection was acquired in C57BL/6 mice where the adult group comprised of 2–9 months old mice. For establishment of the protocol, the distribution of [^{99m}Tc]Tc-diethylenetriamine pentaacetate (DTPA) and [^{64}Cu]Cu-human serum

albumin (HSA) was comparatively evaluated on adult mice. Evans Blue and [^{64}Cu]Cu-HSA were used to evaluate the distribution of tracer under various speed and volume conditions. Thereafter the protocol was applied on an aged group comprising of 15–25 months old mice. The clearance parameters were compared.

Results

[^{99m}Tc]Tc-DTPA was not a suitable tracer for evaluation of lymphatic efflux of CSF as no cervical lymph node uptake was observed while it was cleared from the body. A total volume of 3 to 9 μL at an infusion rate of 300 to 500 nL/min was not sufficient for the tracer to reach the cranial subarachnoid space and clear throughout the MLV. As a result, whole-body positron emission tomography (PET) imaging using [^{64}Cu]Cu-HSA at 700 nL/min, to deliver 6 μL of injected volume, was set for characterization of the CSF to MLV clearance. Through this protocol, the mean (± SD) CSF clearance half-life in adult (n=7) and aged (n=6) mice were to be 93.4 ± 19.7 and 123.3 ± 15.6 min ($p = 0.01$). The CSF cleared slower with an overall higher retention %ID in the aged mice.

Conclusions

A nuclear imaging protocol was established for evaluation of lymphatic efflux of CSF using [^{64}Cu]Cu-HSA and the lymphatic efflux of CSF was confirmed to be delayed in aging mouse model. This protocol can be used for evaluation of preclinical models of brain diseases associated dysfunctional lymphatic efflux of CSF and is expected to be used as a tool to evaluate relationship between lymphatic efflux of CSF and brain diseases in human.

Keywords: Cerebrospinal fluid, Lymphatic efflux, Meningeal lymphatic vessels, Aging, PET, HSA

Student Number: 2019-33343

Table of Contents

List of Figures

List of Tables

List of Abbreviations

Abbreviations	Full name
CSF	Cerebrospinal fluid
DTPA	Diethylenetriamine pentaacetate
EBD	Evans blue dye
HSA	Human serum albumin
ICM	Intra-cisterna-magna
ICP	Intracranial pressure
%ID	Percent of injected dose
ISF	Interstitial fluid
IT	Intrathecal
ITLC	Instant thin layer chromatography
LN	Lymph node
MIP	Maximum intensity projection
MLV	Meningeal lymphatic vessels
MRI	Magnetic Resonance Imaging
PET	Positron emission tomography

ROI	Region of interest
SAS	Subarachnoid space
SD	Standard deviation
SPECT	Single photon emission computed tomography
$t_{1/2}$	Half life

Introduction

Clearance pathways for brain waste materials

The brain waste materials are being increasingly proven responsible for the aging process and the neurodegenerative diseases (1, 2). Those brain wastes materials particularly the macromolecular amyloid beta, extracellular tau, and alpha-synuclein originate from the neurons and glial cells, get disposed into the brain interstitial fluid (ISF), and then traverse the paravascular space to reach the cerebrospinal fluid (CSF) contained within the cerebral ventricles, spinal canal and the subarachnoid space (SAS) (3-6). The sole role of the cranial arachnoid villi for drainage of those macromolecular waste from the CSF directly into the blood of dural venous sinus was doubted with a decades-old assumption that there are alternative routes for clearance (7). The recent confirmations of the anatomic existence of the meningeal lymphatic vessels (MLV) around the venous sinus within the dura mater, and the functional continuity of those MLV to the lymph nodes (LN) in the cervical region suggest a distinct pathway for the clearance of macromolecular brain waste from the CSF (8-12). Similarly, MLV was found in the spinal cord meninges in addition to the spinal arachnoid granulation (13-15). The current understanding about clearance pathways are summarized in figure 1.

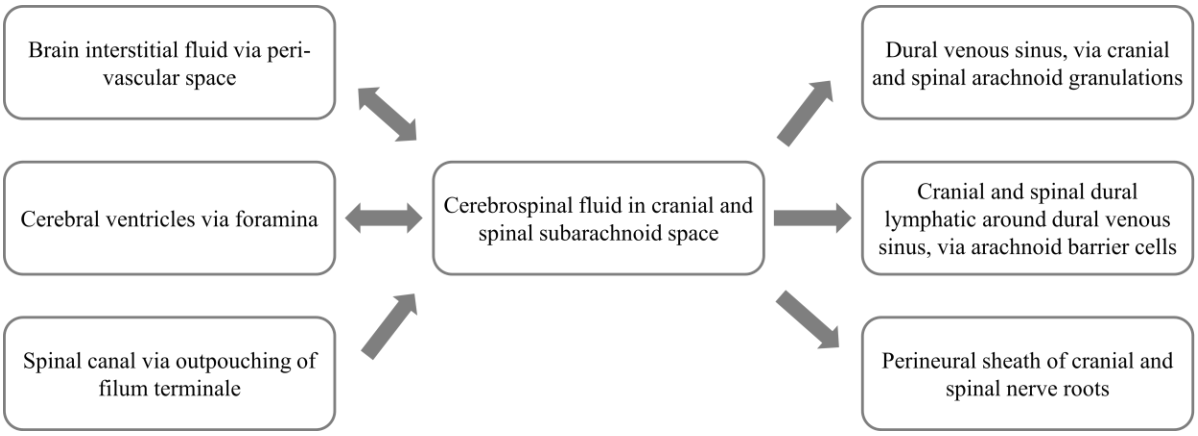

Figure 1. Current understanding about clearance pathways for brain waste material

The strands of evidence suggest that the brain wastes cross the arachnoid barrier cells for a transit through the arachnoid granulation-like dural gap to enter the MLV (14, 16-18). The MLV around the dural sinuses in the dorsal and basal intracranial aspects exits via the foramina and fissures to reach the interconnected superficial and deep cervical LN while the superficial nodes receive additional lymphatics from the nasal mucosa (19-21). The MLV surrounding the spinal cord are arranged in a sparsely interconnected modular fashion within the vertebral canal of each vertebra that exits bilaterally through the intervertebral foramen, circuit around and along the dorsal nerve roots as well as the sympathetic ganglia and then end up in the lymph nodes at the sacral, iliac, lumbar, mediastinal regions, as well as directly to the thoracic duct (22). Taken together, the clearance of CSF contained macromolecular waste via the intracranial and spinal MLV to the cervical and other regional LN can be expressed by the term 'lymphatic efflux of CSF'.

Relevance of clearance pathways in diseases

Induction of experimental dysfunction in the lymphatic efflux either by mechanical ligation of cervical lymphatic conduits or by photoablation following a local administration of photosensitizer agent, lead to a backlog of macromolecular brain waste materials in the CSF and brain interstitial fluid with a concomitant deterioration of cognition in mice models of aging and Alzheimer's (19, 23, 24). The age-related cognitive decline coincides and therefore suggested to be causally associated with the age-related alteration in the phenotypic and transcriptomic features of MLV that leads to a dysfunctional clearance of brain waste in animal models (19). This dysfunction is likely to be further worsened by age-related decline in the contractility of the peripheral lymphatic vessels (25). The dysfunctional lymphatic efflux was also found to play a key role in the pathologic progression of Parkinson's disease (26), hepatic

encephalopathy(27), subarachnoid hemorrhage (28-30), ischemic stroke (31), traumatic brain injury (32, 33) and brain tumors (34, 35)

The alleviation of macromolecular backlog with a concomitant improvement of spatial memory in the aging model undergoing lymphangiogenic treatment with vascular endothelial growth factor (19), along with the proof in human about the connection of MLV along the cranial nerves and cervical LN with age-related phenotypical change of cervical LN and MLV (36), suggest the clinical usefulness of modulation of lymphatic efflux pathways for the treatment of neurological diseases including the age-related neurodegeneration. Moreover, the reduction of amyloid deposition with an improvement of memory performance the Alzheimer's model during blood-brain-barrier modulation even after mechanical ligation (24) supports the utility of lymphatic efflux through the spinal MLV.

Issues in the investigations of clearance pathways

The exploration of the lymphatic efflux of CSF have depended upon *ex-vivo* imaging with fluorescent-dye labelled macromolecules (19, 37, 38), *in-vivo* imaging with gadolinium-labelled magnetic resonance imaging (MRI) contrast agents (39, 40), count based (non-imaging) measurement of radioactivity after infusion of radio-isotope labelled protein (41, 42), and near-infrared imaging (43). Similarly, the clearance pathway through spinal MLV were evaluated with near-infrared imaging (44) as well as *ex-vivo* imaging of decalcified spinal segments with fluorescent-dye labelled macromolecules (22).

The *ex-vivo* technique is advantageous because of the specific labelling of blood vessels and meningeal vessels allow accurate differentiation as well as detail evaluation of structures. However, the technique limits the evaluation within small field of view, although magnified. This precludes the simultaneous assessment of the entirety of lymphatic efflux that extends

throughout the skull and spines. Moreover, the *ex-vivo* technique is incapable of collecting data over multiple time-point from the same animal. Thus, the brain waste clearance being a dynamic physiological process is expected to be better handled by *in-vivo* longitudinal assessment. Moreover, the *in-vivo* method can verify for confounders like group differences and individual variations (45).

The injection of gadolinium contrast into CSF for the magnetic resonance imaging (MRI) of lymphatic efflux, reportedly caused neurotoxicity in animals with an overall adverse event rate of 13% in humans (46). An MRI parameter called the '% change in signal unit ratio' in the cervical LN was so indistinct in comparison to that in the CSF (40), that the requirement for administration of larger volume of gadolinium contrast is inevitable. Thus the interpretability of CSF-lymphatic efflux with contrast enriched MRI seems to be in a conflicting position with the safety recommendations of keeping the MRI contrast infusion at the lower end.

Small animals are vulnerable to suffer from perturbation of their physiological milieu during administration of an exogenous tracer for *in-vivo* studies. The CSF volume and CSF production rate in mice generally known through studies is 36.6 μL and 370 nl/min (47, 48). The reported results for lymphatic efflux of CSF were based upon tracer-infusion volume and rates which were significantly higher than that of the physiological volume and rates of CSF-production (5, 9, 19, 47-56). Reportedly, an infusion of tracer within the CSF compartment at a rate twice that of the physiological rate of CSF production had doubled the intracranial pressure (ICP) in rat models (57, 58). Whereas, an experiment on ovine model discovered a two-fold rise of ICP can cause the CSF efflux rate to rise by several-folds through both the lymphatic and arachnoid villi routes (59). Taken together, an infusion speed higher than the physiological rate of CSF production can lead to an increased CSF efflux resulting in an erroneous discovery of facts.

Applicability of the radionuclide imaging

The translational research on neurodegenerative disease has relied mostly on the mouse models while the use of radionuclides remained confined within *ex-vivo* scintillation counting with the radionuclide imaging remaining noticeably underutilized (60-62). The single-photon emission computed tomography (SPECT) and positron emission tomography (PET) can offer and *in-vivo* assessment of unperturbed physiology in small animal because the injection of radiotracer is made at a sub-pharmacological dose with high specific activity. The SPECT or PET radionuclide cisternography can produce images with a high target-to-background ratio when the radiotracer is injected directly into the CSF compartment (3), which can be useful for qualitative evaluation of lymphatic efflux of CSF with no or minimum perturbation of animal physiology (63). The radionuclide imaging can also overcome the drawbacks of *ex-vivo* imaging by providing multiple time point, *in-vivo* overview of the whole body tracer distribution in small animal.

Purpose

The purpose of this study was firstly to establish a protocol of molecular imaging for the evaluation of lymphatic efflux of CSF in adult mice; thereafter imaging protocol was applied to aged mice to verify the change of lymphatic efflux between young mice and aged mice. The qualitative and quantitative imaging data from both models were statistically compared.

Materials and methods

Selection of radiotracer

The [^{99m}Tc]Tc-diethylenetriamine pentaacetate (DTPA) with a molecular weight of 0.39 kDa was used for SPECT and the [^{64}Cu]Cu-human serum albumin (HSA) with a molecular weight of 66.5 kDa was used for PET imaging.

Radiolabeling of Human Serum Albumin

The human serum albumin was radiolabeled with ^{64}Cu ($t_{1/2}$ = 12.7 hr, β+ = 655 keV 17.8%, β– = 579 keV 38.4%) by click chemistry based method (64) and the scheme for radiolabeling was depicted in Figure 2. Briefly ^{64}Cu in HCl solution was dried with nitrogen flow of 5-10%. Then 1M sodium acetate buffer was added to adjust the pH to 5.3 followed by performance of instant thin layer chromatography (ITLC) using 0.1 M Sodium citrate as the mobile phase. Then N_3-NOTA 13 nml/L, 10 µL was added and the mixture was placed in heater block at 60-70ºC for 10 minutes followed by performance of ITLC using acetonitrile as the mobile phase to check the purity. Then ADIBO-albumin (Human serum Albumin, 66.7 kDa) was added and the mixture was place in orbital shaker for 10 minutes. Thereafter the mixture was transferred to filter fitted tube followed by centrifugation at 15,000 rpm and 7.5ºC for 5 minutes. ITLC was performed once again for the residue and filtrate using acetonitrile as the mobile phase to check the purity of [^{64}Cu]Cu-HSA to be over 99% (figure 3).

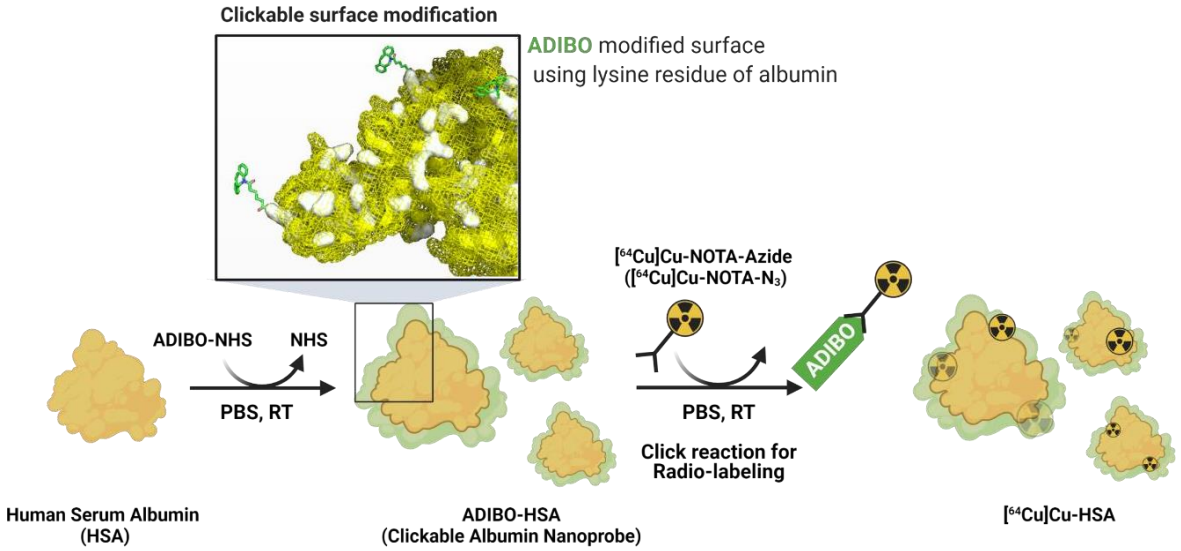

Figure 2. Schematic diagram of click chemistry-based radiolabelling of human serum albumin with ^{64}Cu.

PBS: Phophate buffer saline, NHS: 1 2,5-dioxopyrrolidin-1-y-l4-azidobutanoate, ADIBO-NHS: Azadibenzocyclooctyne NHS ester, N_3-NOTA: 2,2',2''-(2-(4-(3-(3- azidopropyl) thioureido)benzyl)-1,4,7-triazonane-1,4,7 -triyl) triacetic acid

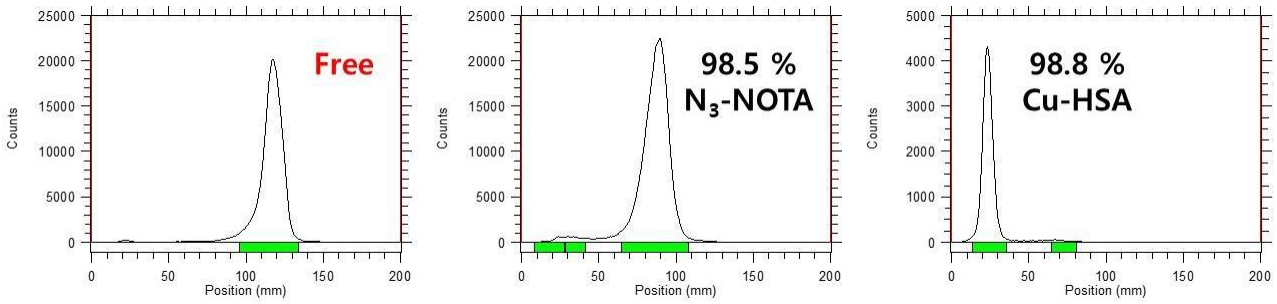

Figure 3. Instant Thin Layer Chromatography results of [^{64}Cu]Cu-HSA

The peak count distributions for free ^{64}Cu, [^{64}Cu]Cu-N_3-NOTA and [^{64}Cu]Cu -HSA are shown

Establishment of imaging protocol

The works were carried out first on the basis of reported methods in the literature. An approach was retained or discarded according to perceived gap between observation and the expected results.

Selection of route for administration of tracer

Firstly, the injection was made through the intrathecal (IT) route following the example of clinical radionuclide cisternography using both the tracers. The intra cisterna magna (ICM) injection was also made using both the tracer following the example of majority of reports that were based on injection of tracer through ICM (5, 8, 9, 19, 22, 37, 49-52, 54, 55, 60, 65-67). The results were evaluated and a the more advantageous one was retained.

Selection of infusion speed and volume for administration of radiotracer

Both the [^{99m}Tc]Tc-DTPA and [^{64}Cu]Cu-HSA were injected IT at an infusion speed of 2 μL/min with the volume being 20 μL following the frequently reported infusion speed and volumes in the literature (table 1). For ICM injection, the [^{99m}Tc]Tc-DTPA was injected first at a rate of 300 nl/min with the volume being 3 μL. The results from the [^{99m}Tc]Tc-DTPA SPECT images guided for a decision to increase the infusion speed to 500 nl/min with the volume being 3 μL for a subsequent [^{64}Cu]Cu-HSA PET imaging.

The infusion speed of 2 μL/min being several fold higher than the physiological rate of CSF production is capable to cause an accelerated lymphatic efflux of CSF. On the other hand, an infusion speed lower than the physiological rate of CSF production can be inadequate to distribute the tracer throughout the SAS, particularly during an IT injection. The distance of

intracranial SAS from the IT injection site at L_3-L_4 inter-vertebral space may be too far for an infusion speed of 300 nl/min to distribute. Moreover, the lymphatic efflux of CSF that occur along the entire length of spinal cord, may lead to an underestimated quantification of lymphatic efflux if the tracer is not distributed adequately within the intracranial SAS during an IT injection. Thus, an *ex-vivo* experiment for inspection of distribution of IT injected tracer was done in order to find out the infusion speed and volume of injection as an optimum trade-off between the physiology and accuracy of quantification.

Evans Blue dye (EBD) is known for avid binding with albumin thus capable of representing the kinetics of albumin in the SAS (68). EBD 2% was suspended in artificial CSF for IT injection for the *ex-vivo* experiment. The infusion speed and volume were set in consideration of the physiological CSF production rate of 350 nl/min in mice (48). Different experimental sets of infusion speeds and volumes were evaluated, 1) 300 nl/min, and 3 μL, 2) 500 nl/min and 3 μL, 3) 600 nl/min and 3 μL, 4) 700 nl/min and 3 μL, and 5) 700 nl/min and 6 μL. The time for EBD infusion varied according to the infusion speed and volume. Cardio-perfusion was started three-minutes after injection was completed and the cardio-perfusion lasted for 15 minutes. Inspection for the distribution of EBD along the dorsal aspect of cervico-thoracic spine, cisterna magna, nasal bone and superficial cervical LN was done before opening the skull. Thereafter, the skull was opened and surfaces of brain, brain-stem and upper cervical spinal cord was inspected for the distribution of EBD. Transverse dissection of spine at cervico-thoracic and thoraco-lumbar regions were made in one case. Photographs were taken.

Table 1 Reported infusion speed and volumes for tracer infusion in the CSF of mice

Publication	**Technique**	**Route**	**Total volume** (μL)	**Rate** (μL/min)
Wang 2020 Sci Transl Med (55)	EVF	ICM	15	1.5
Aspelund 2015 J Exp Med (9), Hablitz 2019 Sci Adv (54)	EVF	ICM	10	2
Iliff 2012 Sci Transl Med (5), Iliff 2013 J Clin Inv (49), Kress 2014 Ann Neurol (51), Smith 2017 eLife (52)	IVTP	ICM	10	2
Iliff 2014 J Neurosci (50)	EVF	ICM	10	1
Xue 2020 Sci Rep (65)	MRI	ICM	7	1
Xie 2013 Science (60), Achariyar 2016 Mol Neurodegener (66) Louveau 2015 Nature (8) Ma 2017 Nat Commun (37)	IVTP EVF NIR	ICM	5	1
Da Mesquita 2018 Nature (19)	MRI	ICM	2-5	2.5
Jacob 2019 Nat Commun (22)	EVF	ICM	2	0.5
Gaberel 2014 Stroke (67)	MRI	ICM	1	1
Wu 2018 J Nanobiotechnology (53)	IVIS	IT	10	Bolus
Jacob 2019 Nat Commun (22)	EVF	IT	2 and 8	1
This study	**RI**	**IT**	**6**	**0.7**

EVF *Ex-vivo* fluorescent microscopy, IVTP *In-vivo* two photon microscopy, MRI Magnetic resonance imaging, NIR Near Infrared Imaging, IVIS *In-vivo* optical imaging, ICM Intra cisterna magna, IT Intrathecal, RI Radionuclide Imaging

Use of anaesthesia

Injection of tracers and image acquisitions were done under inhalational anaesthesia. The animal was first induced with 3% isoflurane with Oxygen flow 500ml/min for ~3 minutes, then placed in a prone position and head away from the operator on a heating pad with its nose inside a gas mask providing 2.8% isoflurane with oxygen flow 500ml/min during the injection. The animal had remained under continuous inhalational anaesthesia during the injection, first session of image acquisition, and wound closure. Thereafter the animal was placed within a cage, placed in a warm place, having access to food and water, and allowed to wake up spontaneously. The animal was induced with anaesthesia for three minutes before each of the upcoming sessions of image acquisition.

Access for tracer injection

For the ICM injection, the palpation of atlanto-occipital joint was done. A 1 × 1 cm area of local skin was shaved, disinfected and then incised. Blunt dissection of the underlying muscles were done to expose the atlanto-occipital membrane. A 31 G needle was inserted. The other end of the needle was connected via a polyethylene tube to a syringe containing the tracer (69). Thereafter the needle was removed, a drop of glue was placed and the wound was closed with 6-0 silk.

For the purpose of IT injection, the L_4 spine was palpated for localizing the site. About 1 × 1 cm area of local skin was shaved, iodine-solution was applied and then a one cm long sagittal incision was made with scissors. Dissection of muscles was avoided with the idea that it helps to reduce the backflow. The needle was inserted through the muscles adjacent to the L_4 spine, in to the space between the L_3 and L_4 spines up to an appropriate length, to feel a resistance that indicates passage through bone and watching for the tail to flick (70). The needle was kept in

place until the first imaging session was over. Thereafter the needle was removed, and the wound was closed with sutures.

CSF injection was made by a syringe pump (Harvard Apparatus), calibrated for the rates and volumes using a 0.5 cc (500 μL) syringe with major graduations of 50 μL and minor graduations of 10 μL. Injection of [^{64}Cu]Cu-HSA was done at the desired rate to deliver a certain volume of total tracer.

Image acquisitions and reconstruction

Whole-body SPECT/ computed tomography (CT) was done using NanoSPECT/CT plus (Mediso). Total 24 projections into an 80 × 80 acquisition matrix were obtained with the frame time being 15 seconds for SPECT acquisition. The SPECT reconstruction used a 3-dimensional ordered-subsets expectation maximum (OSEM) algorithm. The whole-body CT used 55 kVp x-rays with 180 projections, 500 ms of exposure time, and a 1.5 pitch. Genisys PET box (Sofie Biosciences) was used for whole-body PET acquisition of static PET in list mode for 6 minutes at each of the image acquisition time points. The image acquisition time points were at 9-minutes post-injection followed by 2, 4, 6, 12, and 24-hours post-injection for adult mice, whereas the time points for aged mice were at 9-minutes post-injection followed by 2, 4, 6, 17, and 24-hours post-injection. Reconstruction of PET images was automatically done with decay correction by the vendor-provided software that produced the DICOM files.

Image analysis

Analyses are done using the MIM software. A separate 3D region of interest (ROI) was drawn over the entire SAS and the other organs e.g. lymph nodes, heart, and liver. Moreover, the SAS ROI was divided into two parts according to the IT injection point: (a) caudal to injection site

and (b) cranial to injection site; in order to compare the activity in those two ROI in an attempt to understand if the clearance was different between those two regions. The radioactivity within the needle at the injection site was excluded in all cases. Estimated ROI counts were not corrected for the decay because the image was already decay corrected during the reconstruction. The all the ROI counts were normalized against the count from SAS ROI drawn over the image at 9-minutes post-injection (h_0), as percentage of injected dose %ID. The %ID of each time point (h_n/h_0) was then plotted against the corresponding time points to generate the time-%ID curves. The mean and standard error of %ID at a particular time point (in minutes) for a particular ROI from a particular group was used for comparison between the groups.

Statistical analysis

Calculation of clearance half-life ($t_{1/2}$) was done from the time-%ID plots using the GraphPad Prism. CSF clearance was fitted to an exponential function, using the least-squares method, and the coefficient of determination R^2 was used as indicator goodness of fit, with $R^2 > 0.95$ considered to be a good fit. In order to make a comparison of halve lives for clearance of tracer from the SAS between the groups, the unpaired non-parametric Mann Whitney test was adopted. The comparison of the %ID between the groups at a particular time points were done using the same test. The 12-hour time point in adult mice and 17-hour time point in aged mice remained unmatched and therefore were not compared for %ID. However, those time points were used to construct the time-%ID curves.

The CSF clearance parameters of the [^{64}Cu]Cu-HSA were derived using a one phase decay equation: Y = (Y0 - Plateau)*exp(-K*X) + Plateau

Where, **Y0** is the Y value when X (time) is zero. **Plateau** is the Y value at infinite times. **K** is the rate constant, expressed in reciprocal of the X axis time units. **Tau** is the time constant,

computed as the reciprocal of K. **Half-life** is in the time units of the X axis. It is computed as ln(2)/K. **Span** is the difference between Y0 and Plateau along the Y axis.

Animal models

Male C57BL/6 mouse of 2 to 9 months of age was used as adult whereas mice of 15 to 25 months of age were used as aging model (71). They were housed 2-5 per cage with free access to standard food and potable water. The housing room was maintained at a constant temperature of 22 - 24 °C with a 12/12-hour light and dark cycle. Behaviour test using Y-maze (figure 4) revealed difference (Mann Whitney $p < 0.05$) in the spatial memory among the mice belonging to the two groups. Images from seven adult mice and six aged mice were eligible for analysis.

Assessment of in-vivo stability of [^{64}Cu]Cu-HSA

Samples of CSF, blood and urine were collected from adult mice one and four-hours after intrathecal injection of [^{64}Cu]Cu-HSA and ITLC was performed.

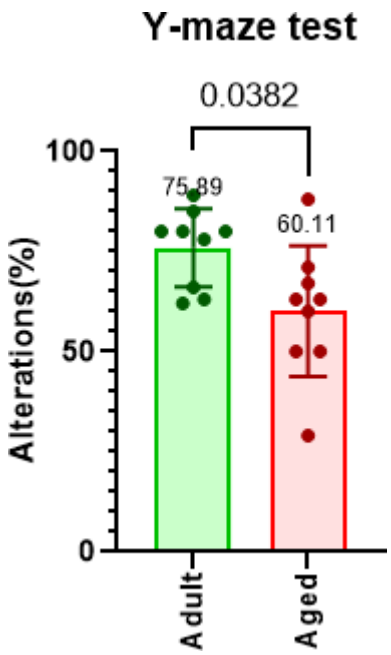

Figure 4. Comparison between mice groups for spatial memory expressed as alterations (%) in a Y-maze

Results

Establishment of imaging protocol

Selection of radiotracer

At first both the radiotracers [^{99m}Tc]Tc-DTPA and [^{64}Cu]Cu-HSA were injected through IT. The [^{99m}Tc]Tc-DTPA was injected with the infusion speed of 2 µL/min for 10 minutes. [^{99m}Tc]Tc-DTPA distributed along the spinal to cranial SAS. However, no cervical lymph nodes uptake of [^{99m}Tc]Tc-DTPA was seen but it was cleared from the body through the urinary tract (Figure.5a). Next, an IT injection of [^{64}Cu]Cu-HSA was made with the same infusion speed of 2 µL/min for 10 minutes. The spinal and cranial SAS was seen and the cervical LNs were visualized as proof of clearance of [^{64}Cu]Cu-HSA from CSF through MLV (Figure. 5b). Thus, [^{64}Cu]Cu-HSA was proven suitable over the [^{99m}Tc]Tc-DTPA for the purpose of evaluation of CSF efflux through lymphatics. The injected radioactivity for the tracers ranged from 0.74 to 1.85 Megabecquerel.

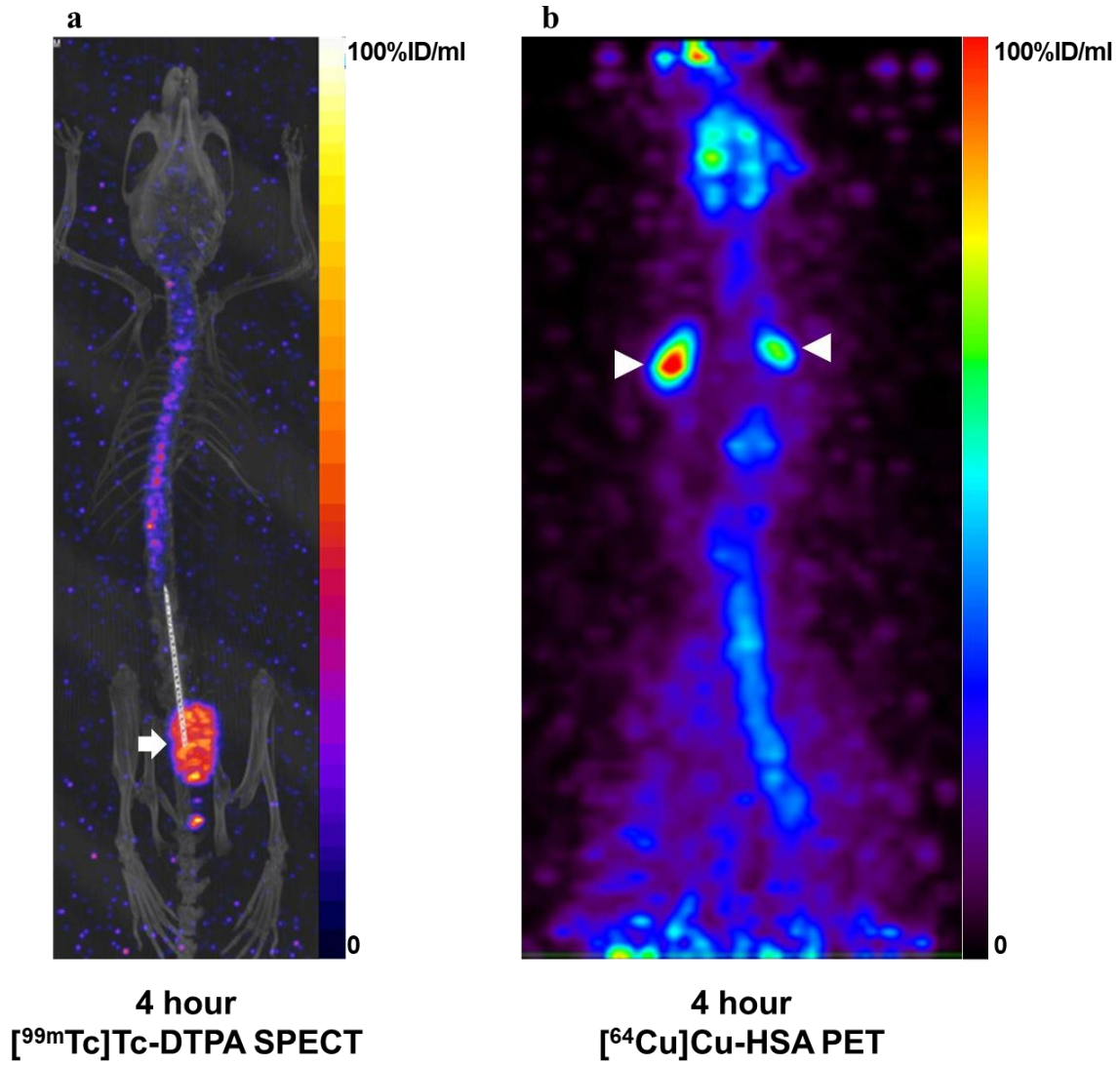

Figure 5. Eligibility of tracer for demonstrating the lymphatic efflux of CSF

Image from [^{99m}Tc]Tc-DTPA fusion SPECT-CT in an adult mice, at 4-hours post-injection showing the tracer inside the spinal SAS and the needle at the injection site. There is a visualization of the urinary bladder, white arrow (a). Image from [^{64}Cu]Cu-HSA PET in another mice, at 4-hours post-injection showing the cranial as well as the spinal subarachnoid space. There is visualization of the cervical lymph node on both sides (arrowheads) in addition to SAS in the basal cranium above and the SAS around spinal cord below (b). The tracer was infused at a rate of 2 µL/min for 10 minutes on both occasions. The colour bar indicates the activity concentration of the tracer.

Validation of injection route for ICM

The injection through ICM route showed substantial back flow of tracer at the site injection with negligible tracer distribution in the SAS, when injected at rate of 300 nl/min with 3 µL of [^{99m}Tc]Tc-DTPA (figure 6a). This backflow was likely due to the pressure of infusion being surpassed of by the pressure and volume CSF at the cisterna magna. The CSF at cisterna magna is known to be continually being joined by the ventricular CSF flow through foramina of Luschka (72).

The backflow persisted despite increment of ICM infusion speed to 500 nl/min with 3 µL of [^{64}Cu]Cu-HSA (figure 6b). Quantification, done in three mice, showed (figure 6c) that the backflow reached up to 50% of %ID over the time. The wide standard deviation (SD) indicate high inter-individual variation. Asymmetrical visualization of cervical LN with rapid clearance from SAS was likely due to the backflow of tracer. The backflow during ICM injection was considered a confounder for accurate quantification of clearance of tracer from SAS. Therefore, the IT injection was chosen over the ICM injection for further experiments.

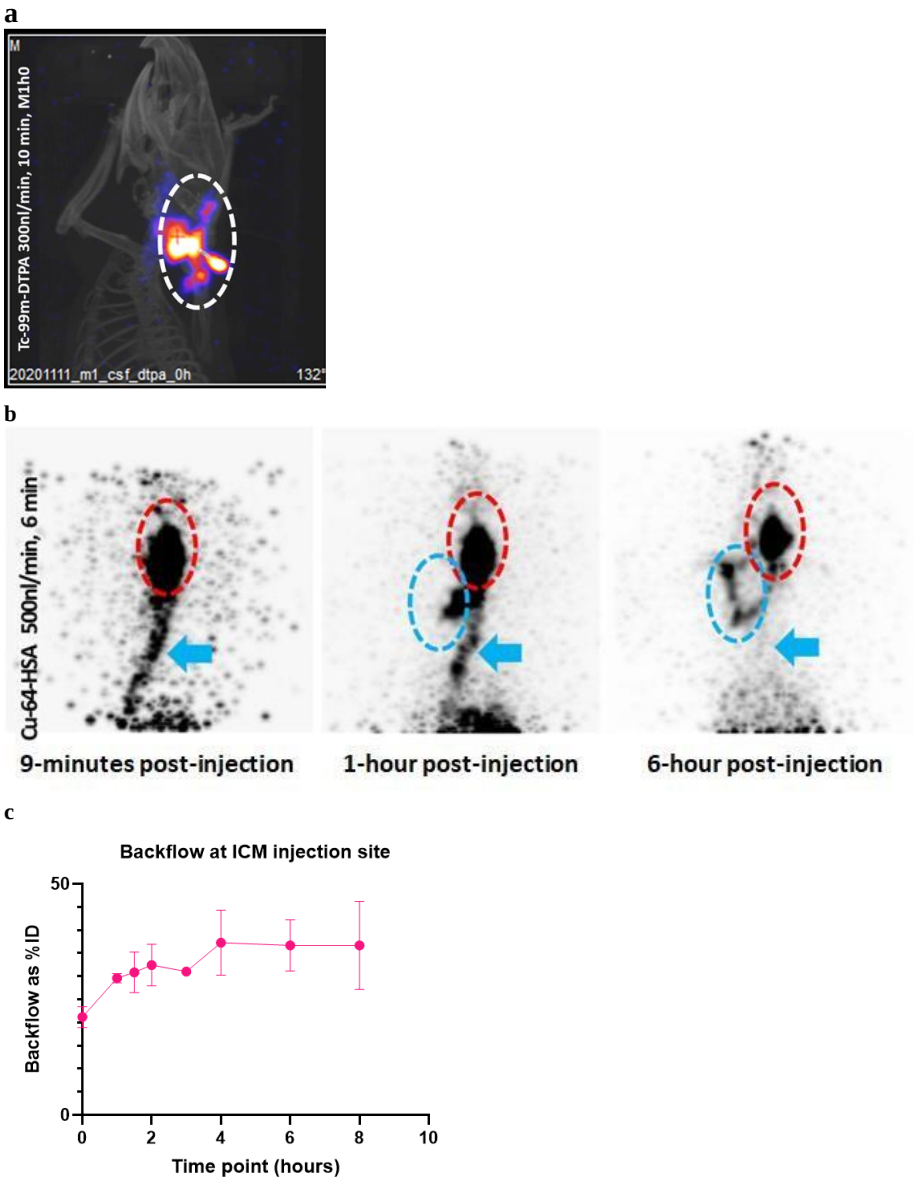

Figure 6. Substantial backflow of tracer at the site ICM injection

Images showing the backflow of [^{99m}Tc]Tc-DTPA, outlined with white ring in the SPECT-CT MIP image in an adult mouse (a). The backflow of [^{64}Cu]Cu-HSA is outlined with red rings in the PET MIP images with the cervical lymph nodes and lymphatic channels marked with blue rings and SAS with blue arrows (b). The quantification of backflow as %ID obtained from [^{64}Cu]Cu-HSA PET in adult mice (n=3).

Selection of optimal infusion speed and volume of IT injection

When EBD in 2% in artificial CSF was injected at an infusion speed of 300 nl/min and volume of 3 μL the EBD did not distribute above the lower thoracic SAS, leaving the cranial SAS devoid of tracer distribution (figure 7a). Therefore, 300 nl/min and 3 μL were considered unsuitable for visualization of lymphatic efflux of CSF through cranial MLV. Subsequently, when the infusion speed was arbitrarily increased to 500 nl/min and a volume of 3 μL was applied, the EBD could distribute up to upper cervical spinal cord with negligible staining of the ventral surface of brain stem (figure 7b). Therefore, 500 nl/min and 3 μL was used for the next [^{64}Cu]Cu-HSA PET imaging.

When [^{64}Cu]Cu-HSA PET was done with IT injection at an infusion speed of 500 nl/min that delivered a total volume of 3 μL, the cranial SAS and the cervical LNs were not visualized until 4-hours post-injection. The heart was visualized (white arrowhead) reflecting clearance of tracer in the systemic circulation likely through lymphatic efflux route other than the one from intracranial MLV to cervical LN (figure 8). Although the infusion speed of 500 nl/min was capable to distribute the EBD within the SAS up to the upper end of cervical cord, the speed was found inadequate for visualization of cranial SAS and cervical lymph nodes during the PET imaging. Therefore, further inspection for *ex-vivo* regional distribution of EBD was done after IT injection at further increased infusion speed and volumes. When the EBD was injected at a speed of 600 and 700 nl/min with the volume of 3 μL, (figure 7c-d) the staining of intact cisterna magna was visible with visible distribution of EBD along the dorsal and ventral surface of brainstem was when the skull was opened. However, the staining of dorso-lateral and ventral surfaces of brain was only seen when the infusion was made a speed of 700 nl/min with the volume increased to 6 μL (figure 7e). The staining of nasal mucosa (red arrowhead) without staining of the superficial cervical LN suggested unlikelihood of accelerated lymphatic efflux by the infusion speed.

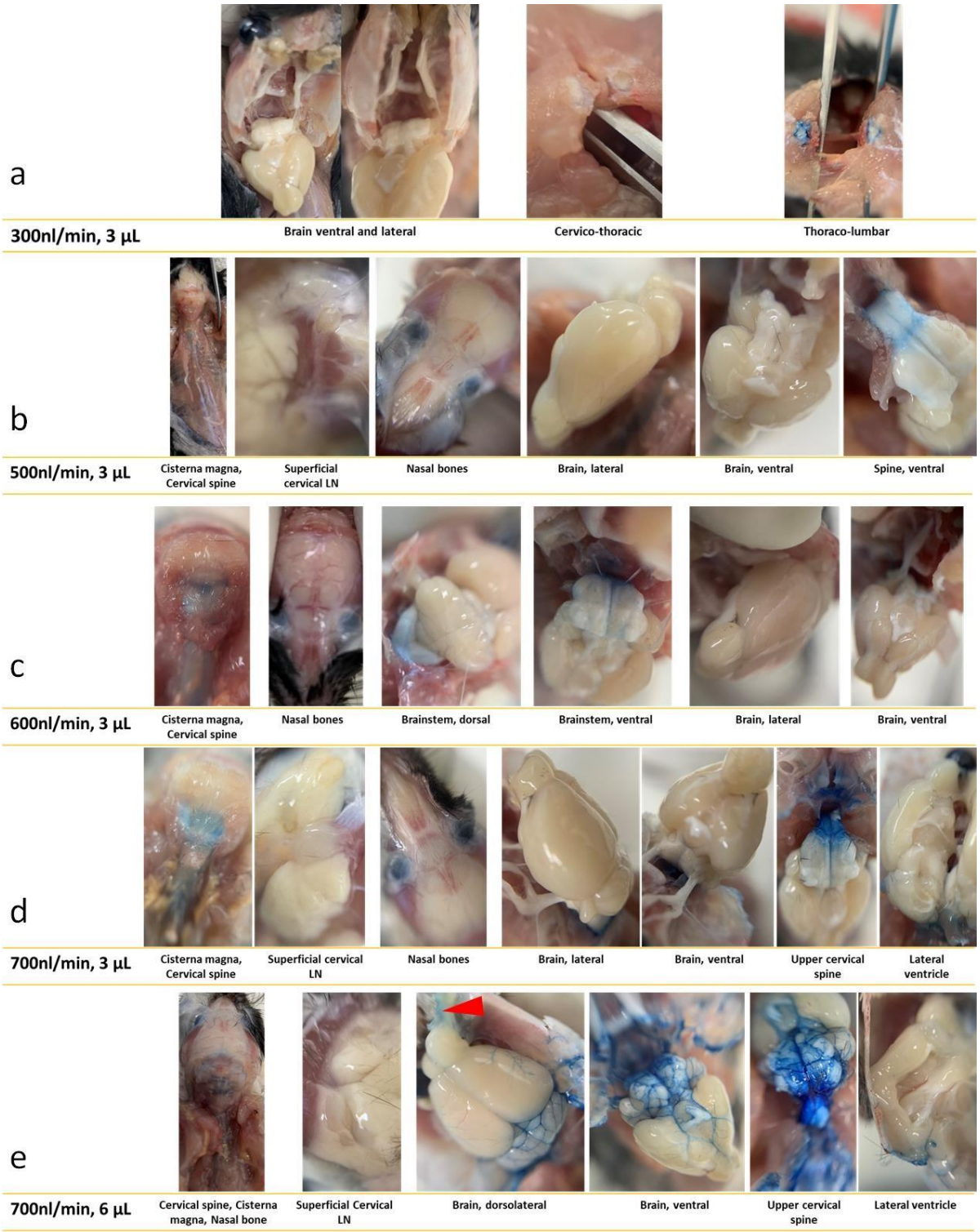

Figure 7. *Ex-vivo* distribution of EBD after IT injection at different infusion speed and volumes

EBD in 2% in artificial CSF was injected in adult mice; photographs were taken after cardio-perfusion with PBS.

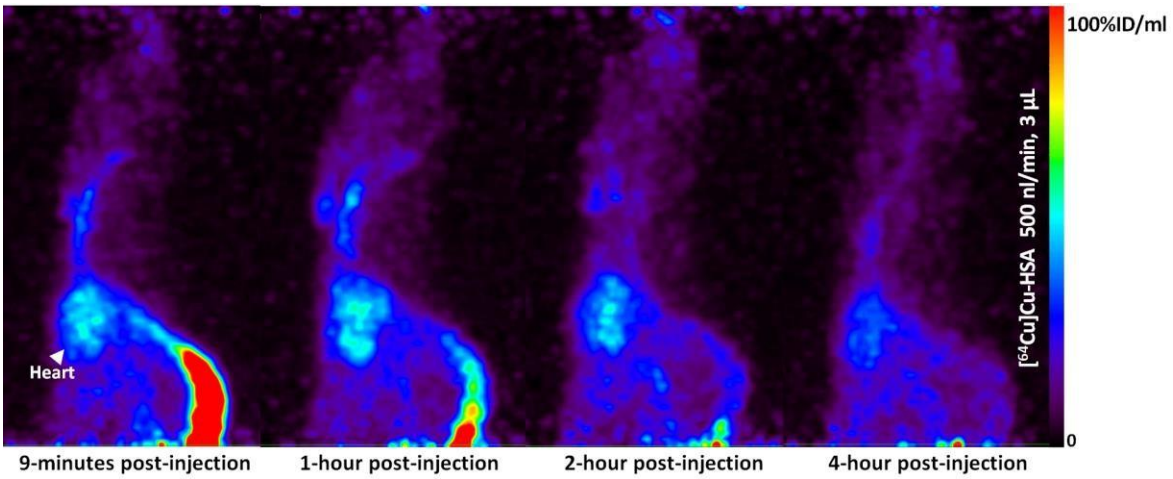

Figure 8. Non-visualization of lymphatic efflux of CSF from cranial SAS with IT injection

PET MIP images in an adult mice after IT injection [^{64}Cu]Cu-HSA using infusion rate of 500 nl/min with the volume being 3 µL, showing non-visualized cervical lymph node, cranial, and cervical SAS. Tracer was seen lower thoracic and upper lumbar SAS. Colour bar on right indicates activity concentration of the tracer

Imaging of lymphatic efflux of CSF in animal models

With the infusion speed further increased to 700 nl/min and the total infused volume being 6 μL, all adult mice showed a similar pattern of distribution of the [^{64}Cu]Cu-HSA in the cranial and spinal SAS, with visualization of cervical (superficial and deep) and pelvic (iliac and sacral) lymph nodes. Figure 9 shows the representative images from 9-minutes as well as the 1, 2, 4, 6, 12, and 24-hours image acquisition time points. At 9-minutes post-injection image, there was intense tracer concentration in the spinal SAS, particularly in the lumbar, thoracic, and cervical segments. The 1-hour image showed gradual dispersion of tracer in the cranial and sacral SAS as well as the superficial and deep cervical LN. The faint activity in the blood pool (heart) and significant activity in the liver was visualized. Activity in the bowel and bladder suggested systemic elimination of tracer through biliary and renal routes respectively. The images from 1 to 6-hours post-injection, showed clearance of activity from the thoracic and cervical SAS to the systemic circulation through cervical, iliac, and sacral LNs and accumulated in the liver. At 12-hours and 24-hours, [^{64}Cu]Cu-HSA was mostly cleared from the SAS with retention of activity in the nasal mucosa, cervical and pelvic LNs, and the sacral SAS.

This same infusion protocol of IT injection with [^{64}Cu]Cu-HSA at speed of 700 nl/min with the infused volume being 6 μL was used to image the CSF to lymphatic efflux in a group of aged mice. Figure 10 shows the representative images from 9-minutes post injection as well as the 1, 2, 4, 6, 17, and 24-hours image acquisition time points. The activity is the SAS was found to be retained indicating slower clearance than the adult mice. The lower liver uptake in aged mice can be attributable to this slower clearance from the SAS leading to slower systemic elimination of the [^{64}Cu]Cu-HSA.

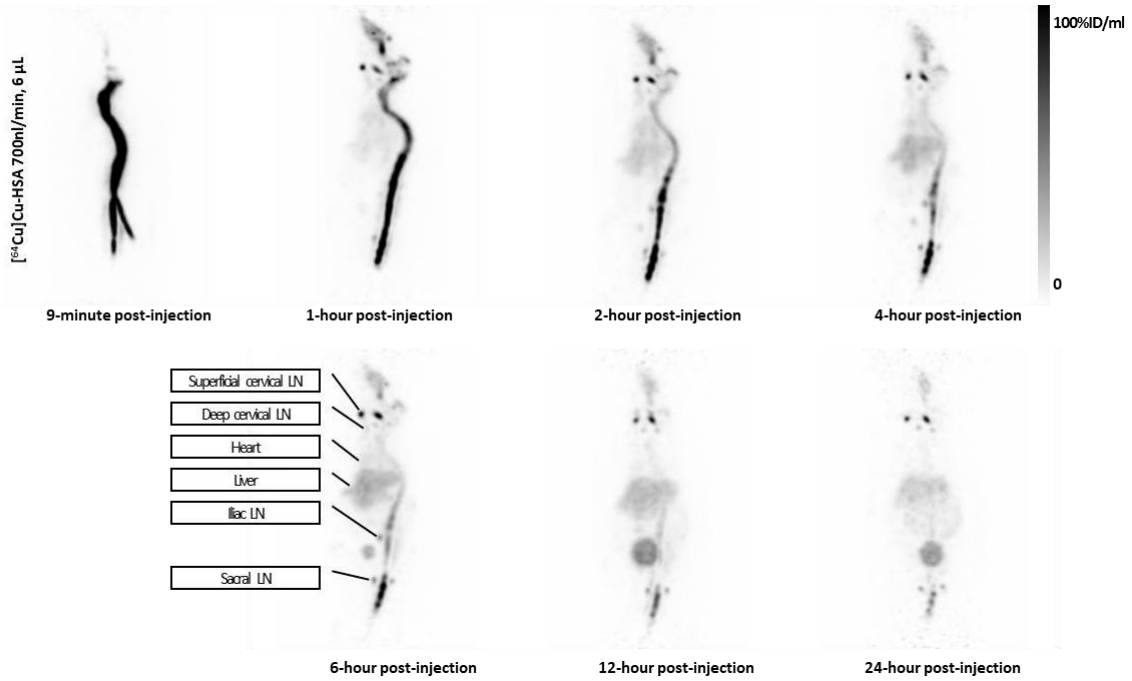

Figure 9. Representative MIP images of whole-body [^{64}Cu]Cu-HSA PET in adult mice

An infusion rate of 700 nl/min was used to deliver a total volume of 6 µL through IT injection in adult mice. The cranial and spinal SAS are seen. The superficial and deep cervical lymph nodes, heart, liver, sacral and iliac lymph nodes are seen. Colour bar on right indicates activity concentration of the tracer**.**

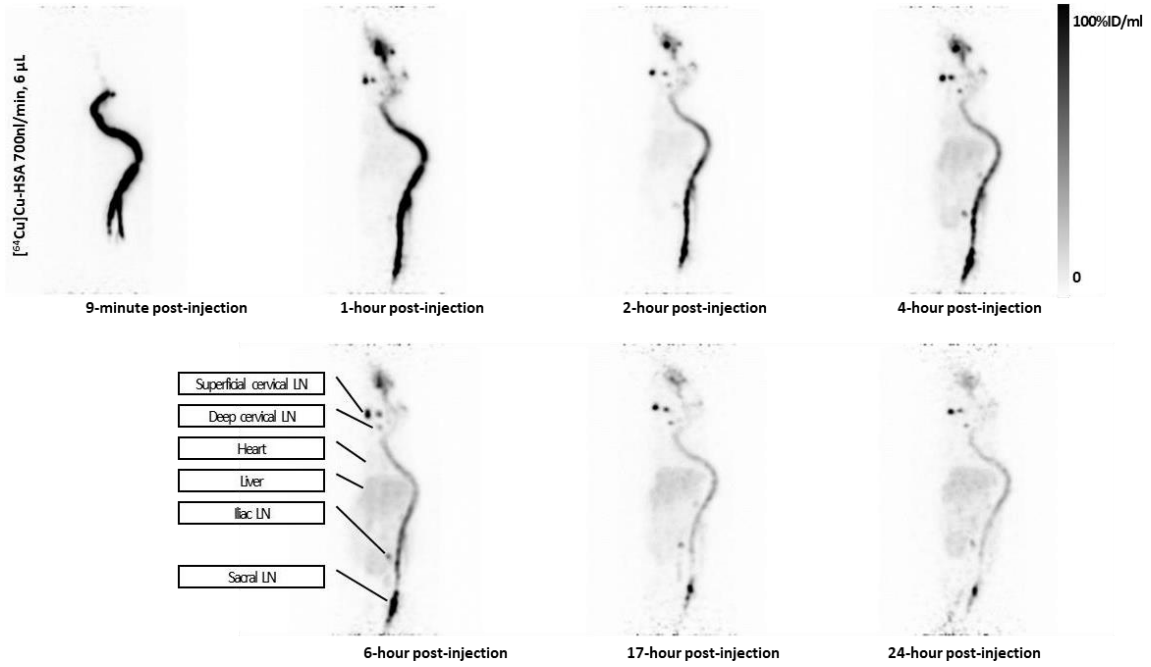

Figure 10. Representative MIP images of whole-body [^{64}Cu]Cu-HSA PET in aged mice

The same infusion rate of 700 nl/min was used to inject a total volume of 6 µL through IT route in aged mouse. The cranial and spinal SAS are seen. The radiotracer uptake in the liver appears to be lower than that in the adult mice and the radiotracer retention in the SAS appears to be higher than that in the adult mice. Colour bar on right indicates activity concentration of the tracer**.**

Comparison of clearance profiles among animal models

The time vs %ID line plots (figure 11) showed an overall temporal decline in the %ID from the entire SAS, representing the 'lymphatic efflux of CSF' in both groups of mice. The clearance parameters of the [^{64}Cu]Cu-HSA , derived from the time-%ID curves are listed in table 2 along with the respective R squared values.

The mean ± SD clearance halve-lives for adult and aged groups were 93.4 ± 19.7 (range 72.3 – 122.2) and 123.3 ± 15.6 (range 97.9-141.4) minutes, respectively. The mean clearance half-life for ages mice were significantly higher than that for adult mice (Mann Whitney $p < 0.05$). The %IDs for aged mice at 4, 6 and 24-hours post injection were also significantly higher than that in adult mice (Mann Whitney $p < 0.05$). Taken together, there was slower clearance or higher retention of tracer in the SAS of aged mice in comparison to the adult mice.

Table 2 Clearance parameters of sub arachnoid space derived from one phase decay equation

	Half Life (min)	R^2	Y0 (%ID)	Plateau (%ID)	K (min^{-1})	Tau (min)	Span (%ID)
Adult mice							
(n=7)	106.6	0.9866	97.75	15.28	0.006501	153.8	82.47
	87.14	0.9853	98.88	13.43	0.007954	125.7	85.45
	72.29	0.9735	96.94	16.16	0.009588	104.3	80.78
	77.36	0.9830	98.22	14.78	0.008959	111.6	83.44
	122.2	0.9873	101.5	14.46	0.00567	176.4	87.05
	111.2	0.9835	102.6	15.77	0.006232	160.5	86.85
	77.05	0.9990	99.96	13.78	0.008996	111.2	86.18
Aged mice							
(n=6)	115.2	0.9660	96.39	24.47	0.006017	166.2	71.91
	141.4	0.9972	99.41	19.55	0.004903	204	79.86
	123.3	0.9880	100.2	21.22	0.005619	178	79
	97.97	0.9902	97.93	20.61	0.007075	141.3	77.32
	125.2	0.9907	101	23.65	0.005536	180.6	77.32
	136.9	0.9804	104.1	19.63	0.005062	197.6	84.48

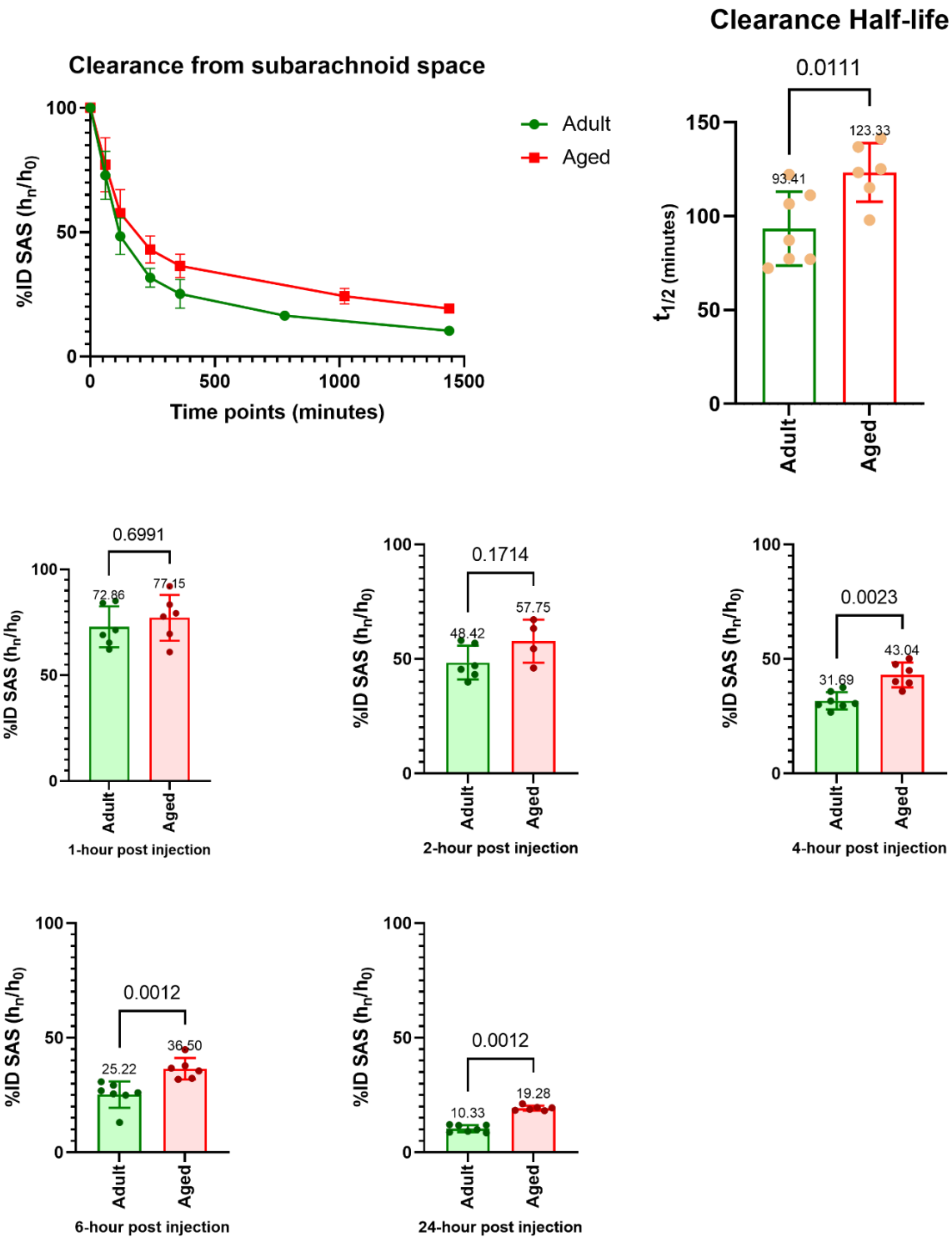

Figure 11. Comparison between mice groups for clearance from entire SAS

The line plot shows comparison of the time-%ID curves and the bar plots show comparison for clearance half-life and the comparison of %ID at the matched time-points.

Figure 12 shows that the difference in %ID between cranial and caudal SAS at 9-minute post injection, became nearly equal during the 1-hour post injection. This happened for both adult and aged mice, indicating an equal clearance of tracer from the SAS segments cranial and caudal to the IT injection site.

Figure 13 shows that there was no difference between the adult and aged mice group when the initial %ID at their respective cranial and caudal segments of SAS were compared ($p = 0.87$ for cranial segment SAS and $p = 0.95$ for caudal segment SAS). The time-%ID plot also shows similar trend for the clearance from the cranial and caudal segment of SAS between the groups.

Figure 14 shows a higher uptake in superficial cervical LN in comparison to that in deep cervical LN at all the time points in both the groups. This may reflect the difference in their received amount of lymphatic efflux of CSF from their corresponding territories in addition to the difference in their sizes. In the adult mice, while %ID in the sacral LN reached an early peak at 2-hours and then started to decline, the %ID in the iliac LN continued to increase until 12 hours. This may support the fact that the lymphatic efflux received by the sacral LN passed through the sacral LN before reaching the systemic circulation in adult mice. On the contrary the %ID in the iliac LN did not surpass the %ID of the sacral LN in aging mice.

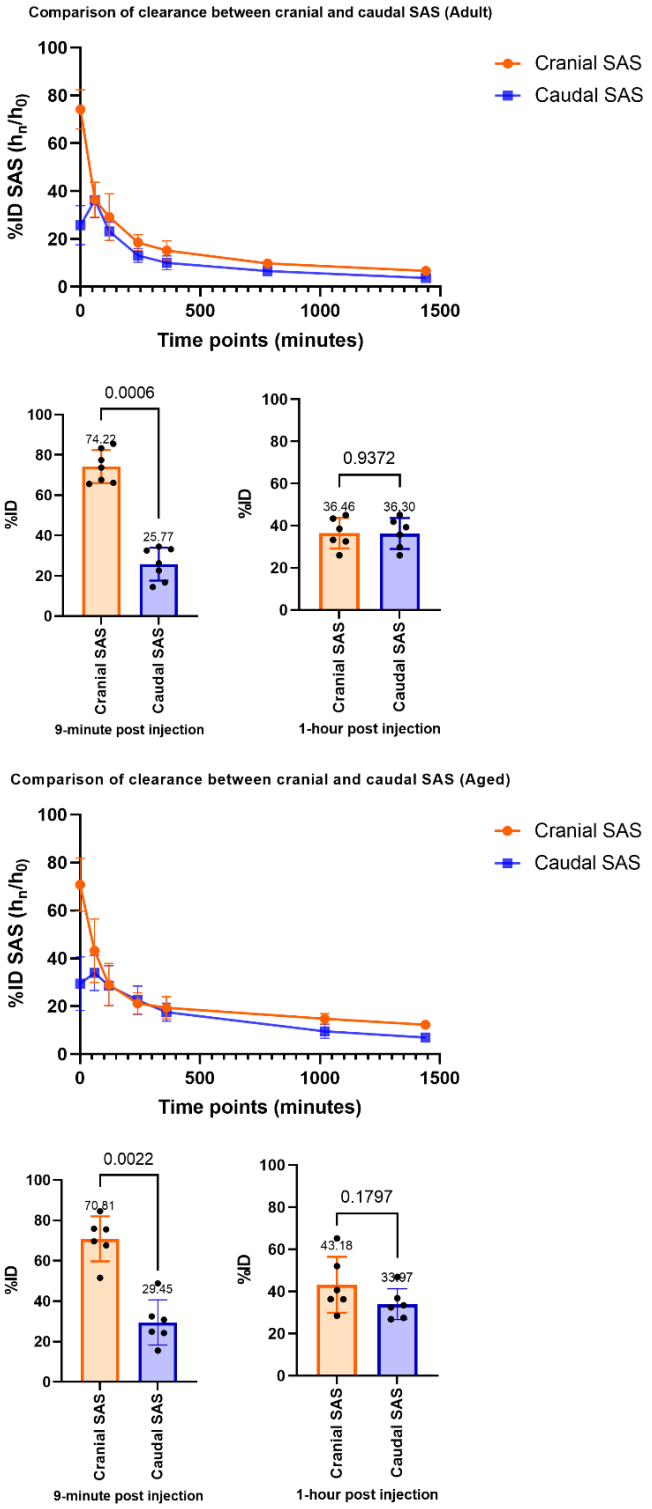

Figure 12. Comparison within mice groups for clearance from the SAS cranial and caudal to the injection site

The line plot shows comparison of the time-%ID curves and the bar plots show comparison for %ID at the initial time-points.

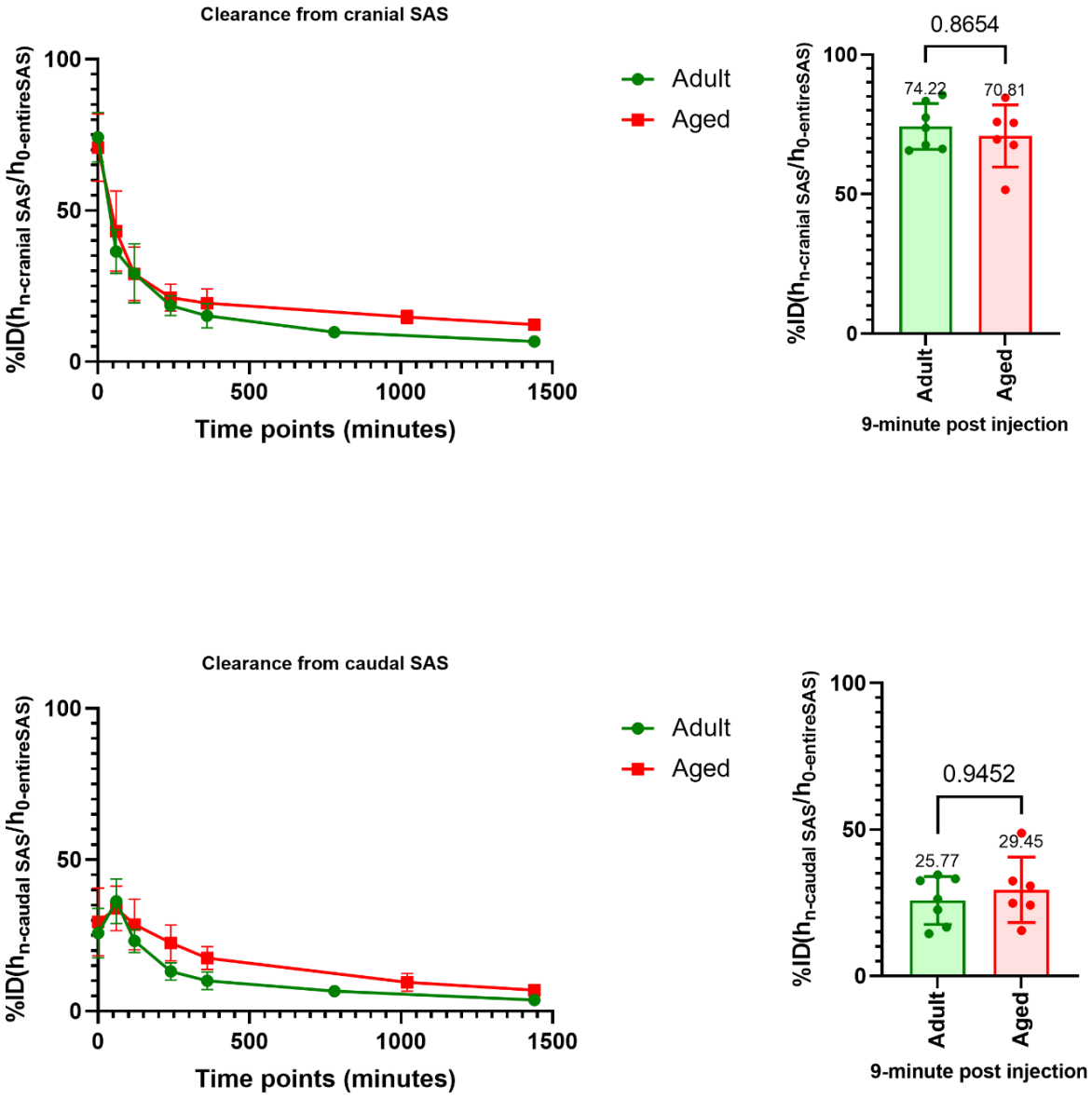

Figure 13. Comparison between mice groups for clearance from the SAS cranial and caudal to the injection site

The line plot shows comparison of the time-%ID curves and the bar plots show comparison for %ID at an initial time-point.

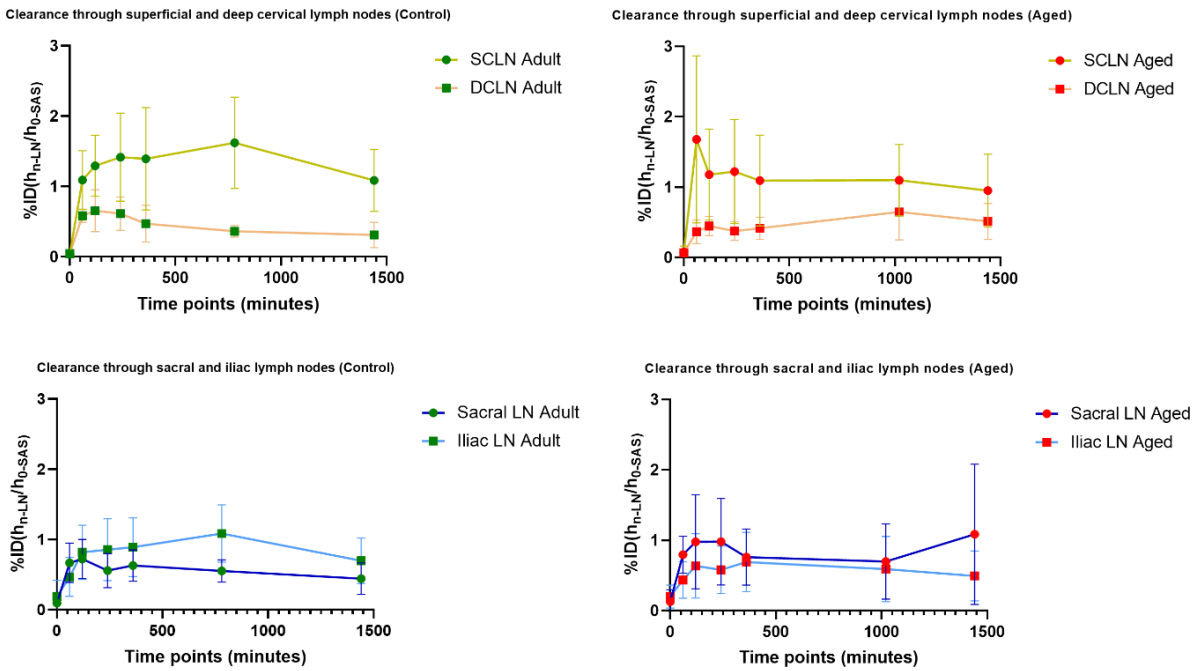

Figure 14. Clearance through the cervical and pelvic lymph nodes

The counts from right and left node from each group were combined to calculate the %ID at each time point for each of the lymph node groups.

The time-%ID curve for liver (figure 15) suggests slightly higher clearance through liver in the adult mice in comparison to the aged mice. However, the %ID remained similar at all the time points in both the mice groups. Similarly, the time-%ID curve for heart (figure 16) suggests slightly prolonged retention of blood pool activity in the aged mice concordant with the higher %ID in the SAS of aged mice at the later time points (figure 11), leading to a persistently elevated blood pool activity. However, no significant difference of the %ID for heart was found at any time point, in comparison to adult mice.

The instant thin layer chromatograms (figure 17) for CSF, blood and urine at 1-hour and 4-hour following the IT injection with chromatograms for the [^{64}Cu]Cu-HSA at the corresponding time-points show single peak for the CSF comprising of greater than 90% of the radioactivity at the origin that represented the intact [^{64}Cu]Cu-HSA. On the contrary, two-peaks of radioactivity was seen in the chromatogram for the blood and the urine, in all the time points where the first peak near to the origin represents intact [^{64}Cu]Cu-HSA, and the second peak toward the solvent-front may represent unbound [^{64}Cu]Cu-N3-NOTA.

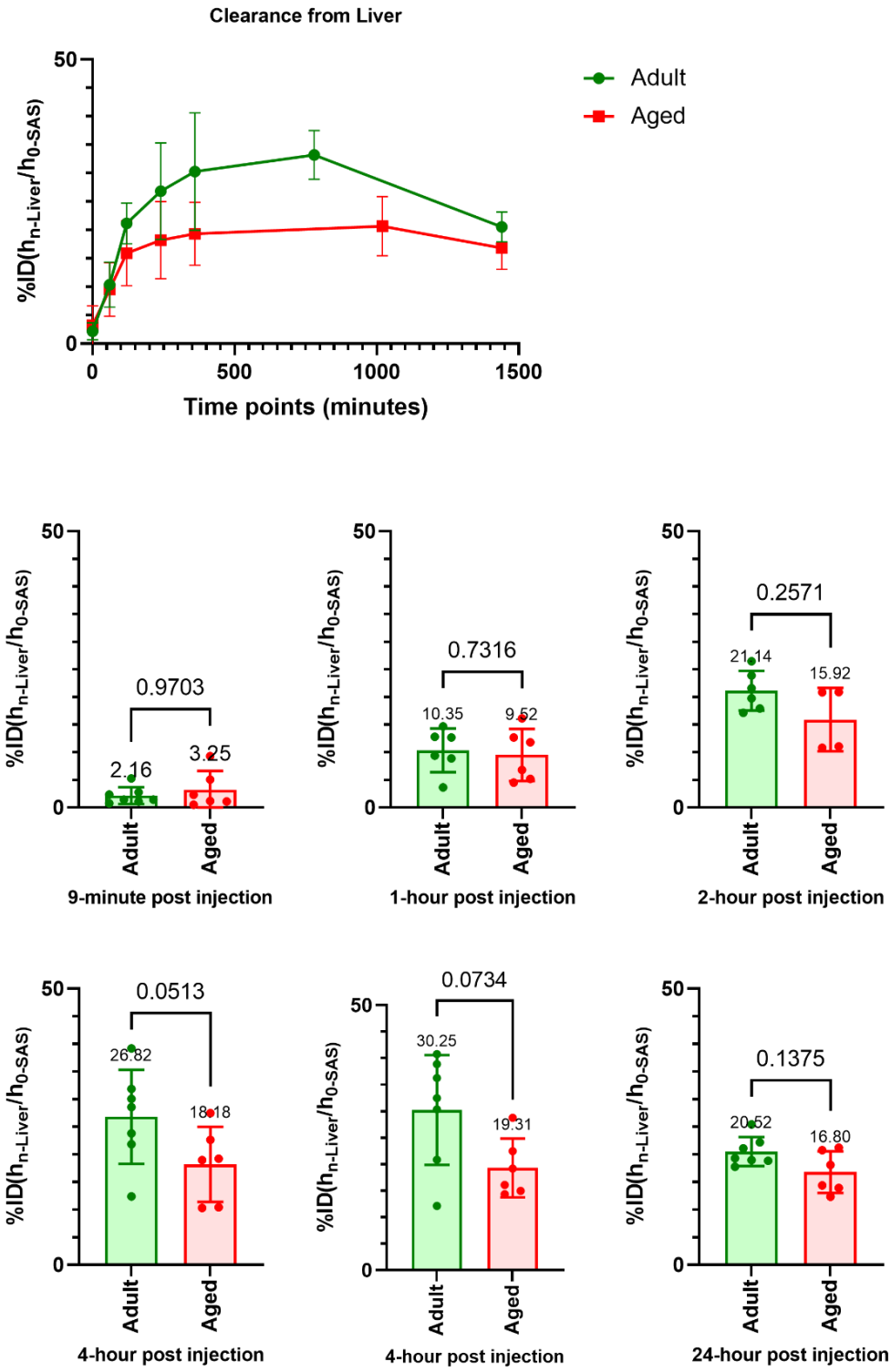

Figure 15. Comparison between mice groups for clearance from the liver

The line plot shows comparison of the time-%ID curves and the bar plots show comparison for %ID at the matched time-points.

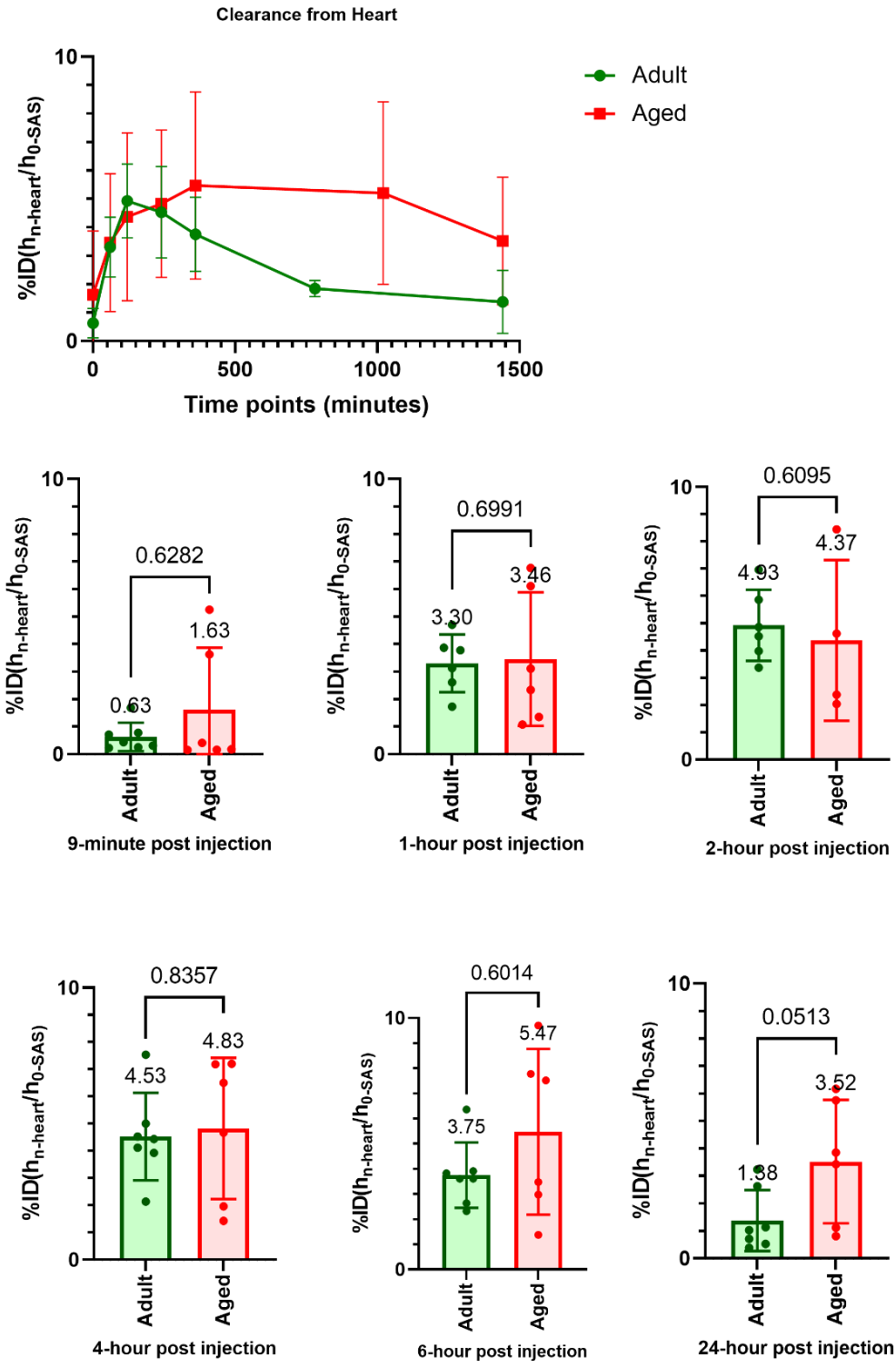

Figure 16. Comparison between mice groups for clearance from the heart

The line plot shows comparison of the time-%ID curves and the bar plots show comparison for %ID at the matched time-points.

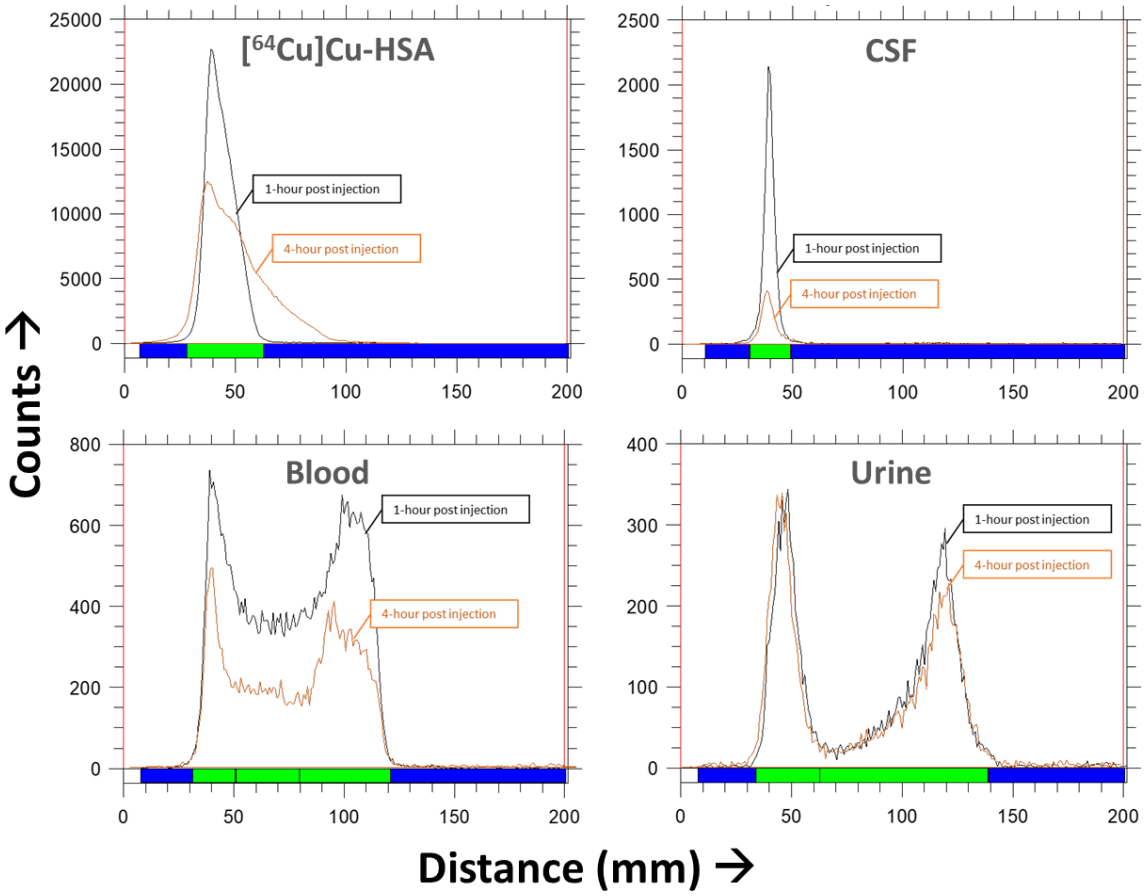

Figure 17. Instant Thin Layer Chromatograms for *in-vivo* stability of [^{64}Cu]Cu-HSA

Discussion

A molecular imaging method was established for the evaluation of lymphatic efflux of CSF using [^{64}Cu]Cu-HSA with the infusion rate of 700 nl/min and the total infused volume of 6 μL. The CSF clearance of the HSA via MLV to LNs and systemic circulation was confirmed in normal mice through the longitudinal acquisition of PET images at multiple time points. An optimal infusion rate and volume for PET imaging was determined by considering the physiological production rate and volume of CSF in mice. The CSF volume and CSF production rate in mice generally known through studies is 36.6 μL and 370 nl/min (47, 48). Accordingly, the infusion rate used in this study was twice higher than the physiological rate of CSF production and the total injected volume reached 16% of the total CSF volume. On the contrary, some of the investigators have used infusion rates of 1-2 μL/min that is 2.9-5.7 times higher than the physiological rate of CSF production and infusion volume of 10-15 μL that reached 25-37.5% of the total CSF volume (5, 9, 19, 48-55) (Table 1).

This was of particular concern because infusion at a rate twice that of the physiological rate of CSF production had doubled the ICP in the rat model (57, 58), while a two-fold rise of ICP in the ovine model caused the CSF drainage rate to rise several-fold higher through both the lymphatic and arachnoid villi routes (59). However, a 2.5 mmHg rise of ICP in mice during cisterna magna infusion using rate and volume of 1 μL/min and 10 μL resulted in about 160% of the ICP at 10 weeks, was claimed to be mild and transient based on the observation of the absence of pathological reflux to ventricles during infusion (56, 73). In addition to the dependence on rate and volume of infusion, the rise of ICP during an intrathecal infusion is subjected to homeostatic pressure-accelerated drainage of CSF into blood (74). Since the immediate post-injection images did not show any evidence of CSF to lymphatic outflow, the infusion rate is likely to have not raised the ICP to a point that would require compensation through pressure-accelerated drainage of CSF. This was concordant with the finding of

minimal stain seen in the nasal mucosa without staining of the superficial cervical lymph node during EBD infusion at 700 nl/min for 6 μL. Thus, the infusion rate and volume used in this study would at least induce less perturbation of the ICP and consequently, physiological changes are expected to be transient and insignificant.

The *in-vivo* PET imaging found the average clearance half-life of HSA from CSF in the entire SAS to be 93.4 minutes when injected at a rate of 700 nl/min to deliver 6 μL of tracer in adult mice. Published data suggest a clearance half-life of 48 minutes using bovine serum albumin radiolabelled with I-125 which was injected IT at a rate of 2.26 μL/min delivering a total volume of 12 μL in adult mice by the ex-vivo scintillation counting of blood-free CSF (48). This 2.5 times higher clearance half-life in adult mice may be attributable to the 70% lower infusion rate and 50% lower infusion volume despite the similar molecular characteristic of the tracer delivered through the same route of administration in this experiment.

The 1.3 times prolonged clearance half-life in aged animals suggested by this experiment is likely to be attributable to age-related alteration in the phenotypic features of MLV and comparable to the twice slower clearance of CSF from the ventricle, albeit with continuous intra-ventricular infusion of Gadospin D, in the aged mice compared to that in the adult mice (75). Similarly, the 2.5 times decline of MLV area coverage and 1.5-2.5 times reduction of tracer deposition in the cervical lymph node, noted after experimental ablation of MLV or ligation of cervical lymphatic conduits (19) can support the fact that an age related dysfunction in CSF to lymphatic clearance was responsible for the prolongation of clearance half-life seen in aged animals in this experiment.

This PET imaging protocol may find further application for verifying the coincident dysfunctional lymphatic efflux of CSF (19) on the experimental models of glymphatic dysfunction in traumatic brain injury and ischemic stroke (50, 67). This protocol may also be applied for *in-vivo* evaluation of dysfunctional lymphatic efflux of CSF which is documented

as a hallmark for progression or exacerbation of neurodegenerative manifestations in the transgenic animals or the experimental animal models of lymphatic dysfunction or the models of other neurodegenerative and chronic systemic diseases (19, 24, 76). Since the clearance of CSF macromolecules through MLV has been a target for therapeutic strategies intended for alleviation of neurodegenerative conditions by locally delivered lymphangiogenic factor (77) or disruption of the blood-brain barrier (24, 78), the protocol reported in the current study may find a role for response evaluation after those novel therapeutic approaches. Click chemistry based radiolabelling of anti-CD4-antibody or cell surface protein of NK-cell, with ^{64}Cu followed by their intrathecal delivery using the protocol, can be a theranostics implication to target the autoreactive $CD4^+$ T-effector cells known for exacerbating the Alzheimer's disease (79) or to study the interaction of exogenous NK cells in aging and transgenic mouse models (80). This protocol with appropriate modification can also have an extended application for the clinical diagnosis of spinal CSF leaks (81), which has diagnostic implication in spontaneous intracranial hypotension. The diagnosis of CSF leak in spontaneous intracranial hypotension has been dependent upon digital subtraction myelography (82, 83) that inadvertently requires two consecutive injections of contrast material and eight exposures of dual-energy CT that imparts a significantly higher effective radiation dose (84, 85) in comparison to the [^{64}Cu]Cu-DOTA-PET cisternography combined with low dose CT (81). The amount of tracer required for intrathecal injection in [^{64}Cu]Cu-DOTA-PET cisternography is significantly lower than the amount of gadolinium based contrast agent for intrathecal MR cisternography and the amount of ^{64}Cu injected was reported to be equivalent to that contained in 0.001 mL of human serum (81). The [^{111}In]In-DTPA cisternography already has a comparable diagnostic performance in comparison to CT or MRI while the [^{64}Cu]Cu-HSA will yield images of higher resolution due the mean energy of ^{64}Cu and the physical half-life of ^{64}Cu will allow imaging at further delayed time-points. All these features will be particularly useful for the cases with slow or intermittent

leakage that are not detectable by digital subtraction myelogram (81) and the cases that requires exclusion of CSF leak because the increased compliance of lower CSF space is rather responsible for the orthostatic headache in patients (86).

In the time-%ID plots from adult mice (figure 14), the %ID in the superficial cervical LN had a steeper rise but higher plateau than the deep cervical lymph nodes. The steeper rise of the %ID in the superficial cervical LN can be an indicator of its receiving lymph at a faster rate, particularly from the nasal mucosa where the CSF tracer is likely to be cleared through the olfactory-perineural route. The higher plateau of the superficial cervical lymph node is due to its much larger size than the deep cervical lymph node that allows accumulation of higher amount radioactivity at all the time points. On the contrary, the sacral LN which is positioned caudally, had a steeper rise but lower plateau that the comparatively cranially placed iliac LN. The steeper rise of the %ID in the sacral LN can be an indicator of its receiving lymph at a faster rate, likely from the lumbar cistern subarachnoid space through the regional vertebral dural and epidural lymphatic connection with the regional peripheral lymphatics conduits. Concordantly, the lower plateau of %ID for the sacral LN along with the less steep rise of %ID but higher plateau for the iliac LN may suggest that the iliac LN was receiving the lymph that contains the CSF tracer from the sacral LN. Taken together, this may point towards a fashion of CSF to lymphatic clearance that occur at the cervical and pelvic regions and hence may be expressed by the term ‘bi-regional clearance’. This bi-regional clearance may be compared with the CSF to lymphatic clearance observed by Ma et al (44) after intra-cerebro-ventricular injection of tracer that cleared through the cervical lymph nodes, moved caudally through the central canal to appear in the CSF of lumbar subarachnoid cistern and then cleared through sacral lymph nodes.

In the aged mice a similar steeper rise of %ID was seen for the superficial cervical LN as well as for the sacral LN. The higher plateau for the superficial cervical LN was also same for the aged mice. However, the plateau for iliac LN was lower in aged mice unlike adult mice, a fact that may indicate slower CSF to lymphatic clearance in aged animal.

Contrarily, the Ma et al (44) have also observed comparable tracer-signal in the thoracic regions when they compared the intra-cerebro-ventricular and the intra-cisterna-magna injections groups, while the tracer-signal in the sacral region was higher in intra-cerebro-ventricular injection group compared to the intra-cisterna-magna injection group. This discrepant clearance can be interpreted as an excretion of the intra-cisterna-magna injected tracer through the thoracic and lumbar regional spinal MLV before it could reach the sacral region while the intra-cerebro-ventricular injected tracer was routed through the central canal to the lumbar cistern without being subjected to any excretion in the thoracic or lumbar regions. Moreover, the anatomical existence of metameric spinal lymphatic with regional connection was confirmed (22, 77) following the long known functional connection between spinal subarachnoid space and the regional perivertebral lymphatic conduits (87). Therefore, the data generated from this experiment cannot precisely differentiate if there was a so called bi-regional clearance or the CSF to lymphatic clearance have occurred through those numerous regional intervertebral outlets. Thus, in order to confirm the *in-vivo* functionality of such spinal MLV, injection of ^{64}Cu labelled nano-particle that are larger than HSA or using 9.4T MRI with Gadospin D can be done in future.

The time-%ID curves for liver indicated accumulation of activity in the liver while there was the appearance of activities in the urinary bladder and colon indicating separation of HSA in liver and kidneys (88, 89) followed by renal and hepatic excretion of [^{64}Cu]Cu-N_3-NOTA. However, the peak for [^{64}Cu]Cu-HSA, in the chromatogram suggests an abnormal excretion of albumin through urine, a phenomenon which is comparable with the previously reported

incidences of albuminuria in mice after intraperitoneal overloading by heterologous albumin of human or bovine origin, at a dose of 250μg to 10 mg/gm body weight (90, 91). The underlying reason for such proteinuria is immune mediated renal ultrastructural inflammatory change that is in turn dependent on antigen-dose, strains and sex (92-97)

The HSA rather than DTPA was selected as the radiotracer for radionuclide molecular imaging of lymphatic efflux. The exploration started with the use of DTPA inspired by its established utility in clinical radionuclide cisternography (3) that has been using intrathecally injected radiolabelled DTPA to visualize the flow of CSF. Moreover, the molecular structure and molecular weight of DTPA (487.2 Da) is similar to that of Gadobutrol (604.7 Da), an agent used for visualization of cervical lymph nodes following IT administration in human (40). In addition, the neurotoxic complication and narrow safety margin for intrathecally administered gadolinium based contrast agents in humans (46) necessitates the selection of DTPA over Gadolinium. However, in this study, no evidence was found for DTPA to pass through MLV until it is cleared from the CSF into the systemic circulation. This clearance of DTPA without visualization of the cervical lymph node can be also attributable to the molecular structure and size of the DTPA which may allow the passage of tracer via the MLV through LN without sequestration, in addition through the venous clearance to reach the systemic circulation (98, 99). This also matches with the fact that cervical LN uptake of radiolabelled-DTPA has never been reported in humans (100, 101). Whereas HSA in addition to being biocompatible (102), has a molecular weight (66.5 kDa) nearly similar to that of 55-62 kDa tau proteins (103).

The hydrodynamic diameter of the [^{64}Cu]Cu-HSA was 8.8 ± 1.4 nm (64), which falls within the range of tau that can reach up to 14 nm (104, 105). Surface charge also affects the lymphatic clearance of the molecule and a denser negative surface charge can confer faster lymphatic clearance (106, 107). [^{99m}Tc]Tc-DTPA, HSA, and phosphorylated tau molecules bear negative surface charges at physiological pH (108-112). Since, the surface charge of HSA becomes more

negative with heightened degree of functionalization during the click chemistry based labelling (64) the net surface charge of [^{64}Cu]Cu-HSA remains similarly negative. Therefore, the size effect is expected to be dominant, and the effect by surface charge is expected to be similar among the molecules. HSA labelling with ^{64}Cu was done using click-based technology which is known for high radiochemical purity and serum stability (64). Moreover, the ITLC at one and four-hour after intra-thecal injection, that demonstrated an excellent *in-vivo* stability of [^{64}Cu]Cu-HSA within the CSF compartment supports the accuracy of the estimated clearance parameters in this experiment. Availability of [^{64}Cu]Cu-HSA in a high specific activity facilitated a high-quality image despite the low volume of tracer injection in this study. The 12.7 hours of half-life of ^{64}Cu allowed longitudinal observation of clearance through multiple time-point over 24-hours.

Indeed, the HSA is known to be immunogenic in mice but the rapid catabolism of HSA in mice results in a rapid decline in the amount of immunogenic HSA after a single injection (113, 114). Given an HSA concentration of 1 μg/μL in the administered tracer, the total administered HSA could have reached 6 μg for one mouse whereas the dose-dependent anaphylactic response leading to death in mice due to xenogeneic albumin required re-injection of 25 μg or higher amount through intravenous route after three weeks of an initial subcutaneous immunization (115). Since a single injection of HSA was made, the issue of immunological reaction at a later time-point is beyond the scope of this study. Furthermore, the final goal being the clinical application of this imaging method the [^{64}Cu]Cu-HSA should be a feasible candidate tracer.

An infusion rate that was either lower or up to twice higher than the physiological rate was insufficient to facilitate the distribution of tracer throughout the SAS after a single injection through the intrathecal route. Concordantly, some investigators who used infusion rates of 0.5 or 1 μL/min with infusion volumes less than 10 μL had a partial observation which was confined either around the cranial or the spinal SAS (8, 22, 37, 60, 65-67) (Table 1).

Contrary to the intra-cisterna magna, the widely used route for tracer delivery, the intrathecal route delivers the tracer at a site where the turbulence of CSF is known to be slow unlike the fast turbulence in the vicinity of cisterna magna owing to the vigorous speed of CSF in the fourth ventricle, ventral surface of the brain stem and cervical SAS (116-118). Therefore, the slow speed of delivery in this experiment could have pushed the tracer steadily towards the rostral direction without any significant regurgitation through the punctured dura at the injection site. Moreover, the resemblance of intrathecal route with that for clinical radionuclide cisternography may favour the translatability of the protocol used in this study.

The use of multiple time points of static image acquisition for short durations under intermittent anaesthesia was preferred over a longer duration of dynamic imaging under continuous anaesthesia primarily because the CSF flow in the spinal SAS, the CSF clearance from spinal SAS to peripheral lymphatic and the contractility of peripheral lymph vessels are significantly inhibited by isoflurane in comparison to the awake condition (44, 119) which altogether can explain the 9-minutes post-injection image (figure 9 and 10) showing faint visualization of cranial and sacral SAS along with non-visualization of peripheral lymph nodes when the animal had been under continuous anaesthesia for intrathecal access followed by the injection and then the image acquisition. Moreover, a 60-minutes period of isoflurane inhalation may cause isoflurane hepatotoxicity (120) and hypothermia (121) leading to fatal cardio-respiratory dysregulation (122).

This PET imaging could find an overall longer clearance half-life in aged mice (table 2 and figure 11) whereas the pre-imaging test for spatial memory showed a cognitive decline in aged mice (figure 4). Both the facts were concordant with the existing evidence for coincidence of cognitive decline and dysfunctional clearance of brain waste in aging (19). Thus the clearance halve-lives and the differences in %ID particularly at 4, 6 or 24-hours post injection can be considered as imaging biomarkers for dysfunctional lymphatic efflux of CSF. The lack of

statistical difference at 1-hour post injection %ID in the SAS caudal and cranial to injection site in both the adult and aged mice indicates attainment of a uniform distribution followed by a similar clearance which in turn supports the non-perturbation of CSF flow by the tracer infusion speed and tracer volume used in the protocol. The %ID in the SAS cranial to injection site was slightly higher throughout the period of evaluation (figure 12) because the volume of SAS cranial to injection site comprised the cranial SAS and the spinal SAS above the level of L3-L4 and therefore was larger than the volume of spinal SAS caudal to the level of L3-L4. Although there was a lack of statistical difference between the mice groups for the clearance from SAS cranial and caudal to the injection site, there was an apparent trend of slower clearance from the aged mice indicated by the slightly higher %D at the later time points on the time-%ID line plots (figure 13).

Although the visualization of lymph nodes confirms the lymphatic efflux of CSF, there was no discernible difference between the groups for the %ID in the lymph nodes at any time point. Although the %ID in the liver of aged mice remaining lower than the adult as well as the %ID in the heart of aged mice remaining higher than the adult, particularly at the later time points tends to comply with the slower clearance from SAS in aging, the difference in the %ID of liver and heart did not reach a statistical significance between the groups at any time point.

Limitations of this study include the inability to establish a protocol that uses tracer infusion at a rate that is lower than or equal to the physiological rate of CSF production and can claim zero perturbation of homeostasis. Since the ICP in mice was not measured, the change of ICP during infusion and the duration of ICP remaining changed cannot be documented. The diurnal variation of lymphatic efflux of CSF (123) could not be separately demonstrated in this study because the study lasted over 24 hours which confers consecutive inclusion of both the dark and light cycles. The results of this study could only suggest a difference of clearance halve lives between groups comprising of two particular ages. Thus, further study is needed to

determine age-specific cut-offs or ranges for the clearance half-life. No variation was found between the groups for clearance profile through the lymph nodes, liver and heart.

Conclusions

In conclusion, a PET imaging protocol was established for the evaluation of lymphatic efflux in normal mice, and the protocol when applied in aged mice, a significant difference in the overall SAS clearance half-life between the two groups along with differences in the SAS %ID at the later time points were noted. This protocol may have utility in the evaluation of preclinical disease models and may evolve as a clinical modality with appropriate modification.

References

1. Ding J, Ji J, Rabow Z, Shen T, Folz J, Brydges CR, et al. A metabolome atlas of the aging mouse brain. Nat Commun. 2021;12(1):6021.

2. Panyard DJ, Kim KM, Darst BF, Deming YK, Zhong X, Wu Y, et al. Cerebrospinal fluid metabolomics identifies 19 brain-related phenotype associations. Commun Biol. 2021;4(1):63.

3. Lee DS, Suh M, Sarker A, Choi Y. Brain Glymphatic/Lymphatic Imaging by MRI and PET. Nucl Med Mol Imaging. 2020;54(5):207-23.

4. Da Mesquita S, Fu Z, Kipnis J. The Meningeal Lymphatic System: A New Player in Neurophysiology. Neuron. 2018;100:375-88.

5. Iliff JJ, Wang M, Liao Y, Plogg BA, Peng W, Gundersen GA, et al. A paravascular pathway facilitates CSF flow through the brain parenchyma and the clearance of interstitial solutes, including amyloid β. Sci Transl Med. 2012;4.

6. Saker E, Henry BM, Tomaszewski KA, Loukas M, Iwanaga J, Oskouian RJ, et al. The Human Central Canal of the Spinal Cord: A Comprehensive Review of its Anatomy, Embryology, Molecular Development, Variants, and Pathology. Cureus. 2016;8(12):e927.

7. Kida S, Pantazis A, Weller RO. CSF drains directly from the subarachnoid space into nasal lymphatics in the rat. Anatomy, histology and immunological significance. Neuropathol Appl Neurobiol. 1993;19(6):480-8.

8. Louveau A, Smirnov I, Keyes TJ, Eccles JD, Rouhani SJ, Peske JD, et al. Structural and functional features of central nervous system lymphatic vessels. Nature. 2015;523(7560):337-41.

9. Aspelund A, Antila S, Proulx ST, Karlsen TV, Karaman S, Detmar M, et al. A dural lymphatic vascular system that drains brain interstitial fluid and macromolecules. J Exp Med. 2015;212:991-9.

10. Koh L, Zakharov A, Johnston M. Integration of the subarachnoid space and lymphatics: is it time to embrace a new concept of cerebrospinal fluid absorption? Cerebrospinal Fluid Res. 2005;2:6.

11. Bucchieri F, Farina F, Zummo G, Cappello F. Lymphatic vessels of the dura mater: a new discovery? J Anat. 2015;227(5):702-3.

12. Sandrone S, Moreno-Zambrano D, Kipnis J, van Gijn J. A (delayed) history of the brain lymphatic system. Nat Med. 2019;25(4):538-40.

13. Hugh AE. The subdural space of the spine: A lymphatic sink? Myodil's last message. Clin Anat. 2010;23(7):829-39.

14. Kido DK, Gomez DG, Pavese AM, Jr., Potts DG. Human spinal arachnoid villi and granulations. Neuroradiology. 1976;11(5):221-8.

15. Miura M, Kato S, Von Lüdinghausen M. Lymphatic drainage of the cerebrospinal fluid from monkey spinal meninges with special reference to the distribution of the epidural lymphatics. Archives of Histology and Cytology. 1998;61:277-86.

16. Nakada T, Kwee IL. Fluid Dynamics Inside the Brain Barrier: Current Concept of Interstitial Flow, Glymphatic Flow, and Cerebrospinal Fluid Circulation in the Brain. Neuroscientist. 2019;25:155-66.

17. Castro Dias M, Mapunda JA, Vladymyrov M, Engelhardt B. Structure and Junctional Complexes of Endothelial, Epithelial and Glial Brain Barriers. Int J Mol Sci. 2019;20(21).

18. Kutomi O, Takeda S. Identification of lymphatic endothelium in cranial arachnoid granulation-like dural gap. Microscopy (Oxf). 2020;69(6):391-400.

19. Da Mesquita S, Louveau A, Vaccari A, Smirnov I, Cornelison RC, Kingsmore KM, et al. Functional aspects of meningeal lymphatics in ageing and Alzheimer's disease. Nature. 2018;560(7717):185-91.

20. Frederick N, Louveau A. Meningeal lymphatics, immunity and neuroinflammation. Curr Opin Neurobiol. 2020;62:41-7.

21. Ahn JH, Cho H, Kim JH, Kim SH, Ham JS, Park I, et al. Meningeal lymphatic vessels at the skull base drain cerebrospinal fluid. Nature. 2019;572(7767):62-6.

22. Jacob L, Boisserand LSB, Geraldo LHM, de Brito Neto J, Mathivet T, Antila S, et al. Anatomy and function of the vertebral column lymphatic network in mice. Nat Commun. 2019;10(1):4594.

23. Wang L, Zhang Y, Zhao Y, Marshall C, Wu T, Xiao M. Deep cervical lymph node ligation aggravates AD-like pathology of APP/PS1 mice. Brain Pathol. 2019;29(2):176-92.

24. Lee Y, Choi Y, Park EJ, Kwon S, Kim H, Lee JY, et al. Improvement of glymphatic-lymphatic drainage of beta-amyloid by focused ultrasound in Alzheimer's disease model. Sci Rep. 2020;10(1):16144.

25. Shang T, Liang J, Kapron CM, Liu J. Pathophysiology of aged lymphatic vessels. Aging (Albany NY). 2019;11(16):6602-13.

26. Zou W, Pu T, Feng W, Lu M, Zheng Y, Du R, et al. Blocking meningeal lymphatic drainage aggravates Parkinson’s disease-like pathology in mice overexpressing mutated α-synuclein. Translational Neurodegeneration. 2019;8(1):7.

27. Hsu S-J, Zhang C, Jeong J, Lee S-i, McConnell M, Utsumi T, et al. Enhanced Meningeal Lymphatic Drainage Ameliorates Neuroinflammation and Hepatic Encephalopathy in Cirrhotic Rats. Gastroenterology. 2021;160(4):1315-29.e13.

28. Liu Q, Hou C, Zhang H, Fu C, Wang W, Wang B, et al. Impaired meningeal lymphatic vessels exacerbate early brain injury after experimental subarachnoid hemorrhage. Brain Res. 2021;1769:147584.

29. Pu T, Zou W, Feng W, Zhang Y, Wang L, Wang H, et al. Persistent Malfunction of Glymphatic and Meningeal Lymphatic Drainage in a Mouse Model of Subarachnoid Hemorrhage. Exp Neurobiol. 2019;28(1):104-18.

30. Chen J, Wang L, Xu H, Xing L, Zhuang Z, Zheng Y, et al. Meningeal lymphatics clear erythrocytes that arise from subarachnoid hemorrhage. Nat Commun. 2020;11(1):3159.

31. Yanev P, Poinsatte K, Hominick D, Khurana N, Zuurbier KR, Berndt M, et al. Impaired meningeal lymphatic vessel development worsens stroke outcome. J Cereb Blood Flow Metab. 2020;40(2):263-75.

32. Bolte AC, Dutta AB, Hurt ME, Smirnov I, Kovacs MA, McKee CA, et al. Meningeal lymphatic dysfunction exacerbates traumatic brain injury pathogenesis. Nature Communications. 2020;11(1):4524.

33. Plog BA, Dashnaw ML, Hitomi E, Peng W, Liao Y, Lou N, et al. Biomarkers of Traumatic Injury Are Transported from Brain to Blood via the Glymphatic System. The Journal of Neuroscience. 2015;35(2):518.

34. Hu X, Deng Q, Ma L, Li Q, Chen Y, Liao Y, et al. Meningeal lymphatic vessels regulate brain tumor drainage and immunity. Cell Research. 2020;30(3):229-43.

35. Song E, Mao T, Dong H, Boisserand LSB, Antila S, Bosenberg M, et al. VEGF-C-driven lymphatic drainage enables immunosurveillance of brain tumours. Nature. 2020;577(7792):689-94.

36. Albayram MS, Smith G, Tufan F, Tuna IS, Bostanciklioglu M, Zile M, et al. Non-invasive MR imaging of human brain lymphatic networks with connections to cervical lymph nodes. Nat Commun. 2022;13(1):203.

37. Ma Q, Ineichen BV, Detmar M, Proulx ST. Outflow of cerebrospinal fluid is predominantly through lymphatic vessels and is reduced in aged mice. Nat Commun. 2017;8.

38. Maloveska M, Danko J, Petrovova E, Kresakova L, Vdoviakova K, Michalicova A, et al. Dynamics of Evans blue clearance from cerebrospinal fluid into meningeal lymphatic vessels and deep cervical lymph nodes. Neurological Research. 2018;40:372-80.

39. Goodman JR, Adham ZO, Woltjer RL, Lund AW, Iliff JJ. Characterization of dural sinus-associated lymphatic vasculature in human Alzheimer's dementia subjects. Brain, Behavior, and Immunity. 2018;73:34-40.

40. Eide PK, Vatnehol SAS, Emblem KE, Ringstad G. Magnetic resonance imaging provides evidence of glymphatic drainage from human brain to cervical lymph nodes. Scientific Reports. 2018;8.

41. Bradbury MW, Cole DF. The role of the lymphatic system in drainage of cerebrospinal fluid and aqueous humour. The Journal of Physiology. 1980;299:353-65.

42. Boulton M, Flessner M, Armstrong D, Hay J, Johnston M. Determination of volumetric cerebrospinal fluid absorption into extracranial lymphatics in sheep. American Journal of Physiology - Regulatory Integrative and Comparative Physiology. 1998;274:R88-96.

43. Ma Q, Ries M, Decker Y, Müller A, Riner C, Bücker A, et al. Rapid lymphatic efflux limits cerebrospinal fluid flow to the brain. Acta Neuropathologica. 2019;137:151-65.

44. Ma Q, Decker Y, Müller A, Ineichen BV, Proulx ST. Clearance of cerebrospinal fluid from the sacral spine through lymphatic vessels. J Exp Med. 2019;216(11):2492-502.

45. Ma D, Holmes HE, Cardoso MJ, Modat M, Harrison IF, Powell NM, et al. Study the Longitudinal in vivo and Cross-Sectional ex vivo Brain Volume Difference for Disease Progression and Treatment Effect on Mouse Model of Tauopathy Using Automated MRI Structural Parcellation. Front Neurosci. 2019;13:11.

46. Patel M, Atyani A, Salameh JP, McInnes M, Chakraborty S. Safety of Intrathecal Administration of Gadolinium-based Contrast Agents: A Systematic Review and Meta-Analysis. Radiology. 2020;297(1):75-83.

47. Oshio K, Watanabe H, Song Y, Verkman AS, Manley GT. Reduced cerebrospinal fluid production and intracranial pressure in mice lacking choroid plexus water channel Aquaporin-1. FASEB J. 2005;19(1):76-8.

48. Rudick RA, Zirretta DK, Herndon RM. Clearance of albumin from mouse subarachnoid space: a measure of CSF bulk flow. J Neurosci Methods. 1982;6(3):253-9.

49. Iliff JJ, Lee H, Yu M, Feng T, Logan J, Nedergaard M, et al. Brain-wide pathway for waste clearance captured by contrast-enhanced MRI. J Clin Invest. 2013;123:1299-309.

50. Iliff JJ, Chen MJ, Plog BA, Zeppenfeld DM, Soltero M, Yang L, et al. Impairment of glymphatic pathway function promotes tau pathology after traumatic brain injury. J Neurosci. 2014;34:16180-93.

51. Kress BT, Iliff JJ, Xia M, Wang M, Wei HS, Zeppenfeld D, et al. Impairment of paravascular clearance pathways in the aging brain. Ann Neurol. 2014;76:845-61.

52. Smith AJ, Yao X, Dix JA, Jin BJ, Verkman AS. Test of the 'glymphatic' hypothesis demonstrates diffusive and aquaporin-4-independent solute transport in rodent brain parenchyma. eLife. 2017;6.

53. Wu PC, Shieh DB, Hsiao HT, Wang JC, Lin YC, Liu YC. Magnetic field distribution modulation of intrathecal delivered ketorolac iron-oxide nanoparticle conjugates produce excellent analgesia for chronic inflammatory pain. J Nanobiotechnology. 2018;16(1):49.

54. Hablitz LM, Vinitsky HS, Sun Q, Stæger FF, Sigurdsson B, Mortensen KN, et al. Increased glymphatic influx is correlated with high EEG delta power and low heart rate in mice under anesthesia. Sci Adv. 2019;5.

55. Wang X, Lou N, Eberhardt A, Yang Y, Kusk P, Xu Q, et al. An ocular glymphatic clearance system removes β-amyloid from the rodent eye. Sci Transl Med. 2020;12.

56. Moazen M, Alazmani A, Rafferty K, Liu ZJ, Gustafson J, Cunningham ML, et al. Intracranial pressure changes during mouse development. J Biomech. 2016;49(1):123-6.

57. Chiu C, Miller MC, Caralopoulos IN, Worden MS, Brinker T, Gordon ZN, et al. Temporal course of cerebrospinal fluid dynamics and amyloid accumulation in the aging rat brain from three to thirty months. Fluids Barriers CNS. 2012;9(1):3.

58. Yang L, Kress BT, Weber HJ, Thiyagarajan M, Wang B, Deane R, et al. Evaluating glymphatic pathway function utilizing clinically relevant intrathecal infusion of CSF tracer. J Transl Med. 2013;11:107.

59. Boulton M, Armstrong D, Flessner M, Hay J, Szalai JP, Johnston M. Raised intracranial pressure increases CSF drainage through arachnoid villi and extracranial lymphatics. Am J Physiol. 1998;275(3):R889-96.

60. Xie L, Kang H, Xu Q, Chen MJ, Liao Y, Thiyagarajan M, et al. Sleep drives metabolite clearance from the adult brain. Science. 2013;342:373-7.

61. Lundgaard I, Lu ML, Yang E, Peng W, Mestre H, Hitomi E, et al. Glymphatic clearance controls state-dependent changes in brain lactate concentration. J Cereb Blood Flow Metab. 2017;37:2112-24.

62. Mestre H, Du T, Sweeney AM, Liu G, Samson AJ, Peng W, et al. Cerebrospinal fluid influx drives acute ischemic tissue swelling. Science. 2020;367(6483).

63. Sarker A, Suh M, Choi Y, Park JY, Kwon S, Kim H, et al. [^{64}Cu]Cu-Albumin Clearance Imaging to Evaluate Lymphatic Efflux of Cerebrospinal Space Fluid in Mouse Model. Nuclear Medicine and Molecular Imaging. 2022.

64. Park JY, Song MG, Kim WH, Kim KW, Lodhi NA, Choi JY, et al. Versatile and Finely Tuned Albumin Nanoplatform based on Click Chemistry. Theranostics. 2019;9(12):3398-409.

65. Xue Y, Liu X, Koundal S, Constantinou S, Dai F, Santambrogio L, et al. In vivo T1 mapping for quantifying glymphatic system transport and cervical lymph node drainage. Sci Rep. 2020;10(1):14592.

66. Achariyar TM, Li B, Peng W, Verghese PB, Shi Y, McConnell E, et al. Glymphatic distribution of CSF-derived apoE into brain is isoform specific and suppressed during sleep deprivation. Mol Neurodegener. 2016;11.

67. Gaberel T, Gakuba C, Goulay R, Martinez De Lizarrondo S, Hanouz J-L, Emery E, et al. Impaired glymphatic perfusion after strokes revealed by contrast-enhanced MRI: a new target for fibrinolysis? Stroke. 2014;45:3092-6.

68. Yao L, Xue X, Yu P, Ni Y, Chen F. Evans Blue Dye: A Revisit of Its Applications in Biomedicine. Contrast Media Mol Imaging. 2018;2018:7628037.

69. Xavier ALR, Hauglund NL, von Holstein-Rathlou S, Li Q, Sanggaard S, Lou N, et al. Cannula Implantation into the Cisterna Magna of Rodents. J Vis Exp. 2018(135).

70. Li D, Li Y, Tian Y, Xu Z, Guo Y. Direct Intrathecal Injection of Recombinant Adeno-associated Viruses in Adult Mice. J Vis Exp. 2019(144).

71. Flurkey K, M. Currer J, Harrison DE. Chapter 20 - Mouse Models in Aging Research. In: Fox JG, Davisson MT, Quimby FW, Barthold SW, Newcomer CE, Smith AL, editors. The Mouse in Biomedical Research (Second Edition). Burlington: Academic Press; 2007. p. 637-72.

72. Liu G, Mestre H, Sweeney AM, Sun Q, Weikop P, Du T, et al. Direct Measurement of Cerebrospinal Fluid Production in Mice. Cell Rep. 2020;33(12):108524.

73. Iliff JJ, Wang M, Zeppenfeld DM, Venkataraman A, Plog BA, Liao Y, et al. Cerebral arterial pulsation drives paravascular CSF-Interstitial fluid exchange in the murine brain. J Neurosci. 2013;33:18190-9.

74. Belov V, Appleton J, Levin S, Giffenig P, Durcanova B, Papisov M. Large-Volume Intrathecal Administrations: Impact on CSF Pressure and Safety Implications. Front Neurosci. 2021;15:604197.

75. Decker Y, Kramer J, Xin L, Muller A, Scheller A, Fassbender K, et al. Magnetic resonance imaging of cerebrospinal fluid outflow after low-rate lateral ventricle infusion in mice. JCI Insight. 2022;7(3).

76. Mentis AA, Dardiotis E, Chrousos GP. Apolipoprotein E4 and meningeal lymphatics in Alzheimer disease: a conceptual framework. Mol Psychiatry. 2021;26(4):1075-97.

77. Antila S, Karaman S, Nurmi H, Airavaara M, Voutilainen MH, Mathivet T, et al. Development and plasticity of meningeal lymphatic vessels. J Exp Med. 2017;214:3645-67.

78. Li MN, Jing YH, Wu C, Li X, Liang FY, Li G, et al. Continuous theta burst stimulation dilates meningeal lymphatic vessels by up-regulating VEGF-C in meninges. Neurosci Lett. 2020;735:135197.

79. Machhi J, Yeapuri P, Lu Y, Foster E, Chikhale R, Herskovitz J, et al. CD4+ effector T cells accelerate Alzheimer's disease in mice. J Neuroinflammation. 2021;18(1):272.

80. Wyatt-Johnson SK, Brutkiewicz RR. The Complexity of Microglial Interactions With Innate and Adaptive Immune Cells in Alzheimer's Disease. Front Aging Neurosci. 2020;12.

81. Freesmeyer M, Schwab M, Besteher B, Gröber S, Waschke A, Drescher R. High-resolution PET cisternography with ^{64}Cu-DOTA for CSF leak detection. Clin Nucl Med. 2019;44:735-7.

82. Schievink WI. Spontaneous Intracranial Hypotension. N Engl J Med. 2021;385(23):2173-8.

83. Schievink WI, Maya MM, Moser F, Prasad R, Wadhwa V, Cruz R, et al. Multiple Spinal CSF Leaks in Spontaneous Intracranial Hypotension: Do They Exist? Neurol Clin Pract. 2021;11(5):e691-e7.

84. Nicholson PJ, Guest WC, van Prooijen M, Farb RI. Digital Subtraction Myelography is Associated with Less Radiation Dose than CT-based Techniques. Clin Neuroradiol. 2021;31(3):627-31.

85. Kim DK, Brinjikji W, Morris PP, Diehn FE, Lehman VT, Liebo GB, et al. Lateral Decubitus Digital Subtraction Myelography: Tips, Tricks, and Pitfalls. AJNR Am J Neuroradiol. 2020;41(1):21-8.

86. Leep Hunderfund AN, Mokri B. Orthostatic headache without CSF leak. Neurology. 2008;71(23):1902-6.

87. Brierley JB, Field EJ. The connexions of the spinal sub-arachnoid space with the lymphatic system. J Anat. 1948;82(Pt 3):153-66.

88. Linder MC, Wooten L, Cerveza P, Cotton S, Shulze R, Lomeli N. Copper transport. Am J Clin Nutr. 1998;67(5 Suppl):965S-71S.

89. Ito S, Fujita H, Narita T, Yaginuma T, Kawarada Y, Kawagoe M, et al. Urinary copper excretion in type 2 diabetic patients with nephropathy. Nephron. 2001;88(4):307-12.

90. Simpson LO, Shand BI. The implications of the changes in the nature of the urinary proteins which occur in albumin overload-induced proteinuria in normal mice. Br J Exp Pathol. 1983;64(1):6-14.

91. Chen A, Wei CH, Sheu LF, Ding SL, Lee WH. Induction of proteinuria by adriamycin or bovine serum albumin in the mouse. Nephron. 1995;69(3):293-300.

92. Lawrence GM, Brewer DB. Studies on the relationship between proteinuria and glomerular ultrastructural change in hyperalbuminaemic female Wistar rats. J Pathol. 1982;138(4):365-83.

93. Donadelli R, Zanchi C, Morigi M, Buelli S, Batani C, Tomasoni S, et al. Protein overload induces fractalkine upregulation in proximal tubular cells through nuclear factor kappaB- and p38 mitogen-activated protein kinase-dependent pathways. J Am Soc Nephrol. 2003;14(10):2436-46.

94. Zoja C, Benigni A, Remuzzi G. Cellular responses to protein overload: key event in renal disease progression. Curr Opin Nephrol Hypertens. 2004;13(1):31-7.

95. Wu CC, Chen JS, Chen SJ, Lin SH, Chen A, Chang LC, et al. Kinetics of adaptive immunity to cationic bovine serum albumin-induced membranous nephropathy. Kidney Int. 2007;72(7):831-40.

96. Chen JS, Chen A, Chang LC, Chang WS, Lee HS, Lin SH, et al. Mouse model of membranous nephropathy induced by cationic bovine serum albumin: antigen dose-response relations and strain differences. Nephrol Dial Transplant. 2004;19(11):2721-8.

97. Ishola DA, Jr., van der Giezen DM, Hahnel B, Goldschmeding R, Kriz W, Koomans HA, et al. In mice, proteinuria and renal inflammatory responses to albumin overload are strain-dependent. Nephrol Dial Transplant. 2006;21(3):591-7.

98. Biceroglu H, Albayram S, Ogullar S, Hasiloglu ZI, Selcuk H, Yuksel O, et al. Direct venous spinal reabsorption of cerebrospinal fluid: a new concept with serial magnetic resonance cisternography in rabbits. J Neurosurg Spine. 2012;16(4):394-401.

99. Ringstad G, Eide PK. Cerebrospinal fluid tracer efflux to parasagittal dura in humans. Nat Commun. 2020;11:1-9.

100. Novotny C, Potzi C, Asenbaum S, Peloschek P, Suess E, Hoffmann M. SPECT/CT fusion imaging in radionuclide cisternography for localization of liquor leakage sites. J Neuroimaging. 2009;19(3):227-34.

101. Verma A, Hesterman JY, Chazen JL, Holt R, Connolly P, Horky L, et al. Intrathecal (99m)Tc-DTPA imaging of molecular passage from lumbar cerebrospinal fluid to brain and periphery in humans. Alzheimers Dement (Amst). 2020;12(1):e12030.

102. Kratz F. Albumin as a drug carrier: design of prodrugs, drug conjugates and nanoparticles. J Control Release. 2008;132(3):171-83.

103. Hirokawa N, Shiomura Y, Okabe S. Tau proteins: the molecular structure and mode of binding on microtubules. J Cell Biol. 1988;107(4):1449-59.

104. Flach K, Hilbrich I, Schiffmann A, Gartner U, Kruger M, Leonhardt M, et al. Tau oligomers impair artificial membrane integrity and cellular viability. J Biol Chem. 2012;287(52):43223-33.

105. Roman AY, Devred F, Byrne D, La Rocca R, Ninkina NN, Peyrot V, et al. Zinc Induces Temperature-Dependent Reversible Self-Assembly of Tau. J Mol Biol. 2019;431(4):687-95.

106. Rao DA, Forrest ML, Alani AW, Kwon GS, Robinson JR. Biodegradable PLGA based nanoparticles for sustained regional lymphatic drug delivery. J Pharm Sci. 2010;99(4):2018-31.

107. Nakamura T, Kawai M, Sato Y, Maeki M, Tokeshi M, Harashima H. The Effect of Size and Charge of Lipid Nanoparticles Prepared by Microfluidic Mixing on Their Lymph Node Transitivity and Distribution. Mol Pharm. 2020;17(3):944-53.

108. Russell CD, Crittenden RC, Cash AG. Determination of net ionic charge on Tc-99m DTPA and Tc-99m EDTA by a column ion-exchange method. J Nucl Med. 1980;21(4):354-60.

109. Alvarez B, Carballal S, Turell L, Radi R. Formation and reactions of sulfenic acid in human serum albumin. Methods Enzymol. 2010;473:117-36.

110. Wegmann S, Biernat J, Mandelkow E. A current view on Tau protein phosphorylation in Alzheimer's disease. Curr Opin Neurobiol. 2021;69:131-8.

111. Alonso AD, Cohen LS, Corbo C, Morozova V, ElIdrissi A, Phillips G, et al. Hyperphosphorylation of Tau Associates With Changes in Its Function Beyond Microtubule Stability. Front Cell Neurosci. 2018;12:338.

112. Tepper K, Biernat J, Kumar S, Wegmann S, Timm T, Hubschmann S, et al. Oligomer formation of tau protein hyperphosphorylated in cells. J Biol Chem. 2014;289(49):34389-407.

113. Low BE, Wiles MV. A Humanized Mouse Model to Study Human Albumin and Albumin Conjugates Pharmacokinetics. Methods Mol Biol. 2016;1438:115-22.

114. Britton S, Celada F. Immunogenicity of human serum albumin: decay in the normal mouse. Immunology. 1968;14(4):503-9.

115. Lei HY, Lee SH, Leir SH. Antigen-induced anaphylactic death in mice. Int Arch Allergy Immunol. 1996;109(4):407-12.

116. Papisov MI, Belov VV, Gannon KS. Physiology of the intrathecal bolus: the leptomeningeal route for macromolecule and particle delivery to CNS. Mol Pharm. 2013;10(5):1522-32.

117. Du Boulay G, O'Connell J, Currie J, Bostick T, Verity P. Further investigations on pulsatile movements in the cerebrospinal fluid pathways. Acta Radiol Diagn (Stockh). 1972;13(0):496-523.

118. Matsumae M, Kuroda K, Yatsushiro S, Hirayama A, Hayashi N, Takizawa K, et al. Changing the Currently Held Concept of Cerebrospinal Fluid Dynamics Based on Shared Findings of Cerebrospinal Fluid Motion in the Cranial Cavity Using Various Types of Magnetic Resonance Imaging Techniques. Neurol Med Chir (Tokyo). 2019;59:133-46.

119. Bachmann SB, Proulx ST, He Y, Ries M, Detmar M. Differential effects of anaesthesia on the contractility of lymphatic vessels in vivo. J Physiol. 2019;597(11):2841-52.

120. Zhu Y, Xiao X, Li G, Bu J, Zhou W, Zhou S. Isoflurane anesthesia induces liver injury by regulating the expression of insulin-like growth factor 1. Exp Ther Med. 2017;13(4):1608-13.

121. Planel E, Richter KE, Nolan CE, Finley JE, Liu L, Wen Y, et al. Anesthesia leads to tau hyperphosphorylation through inhibition of phosphatase activity by hypothermia. J Neurosci. 2007;27(12):3090-7.

122. Frank SM, Fleisher LA, Breslow MJ, Higgins MS, Olson KF, Kelly S, et al. Perioperative maintenance of normothermia reduces the incidence of morbid cardiac events. A randomized clinical trial. JAMA. 1997;277(14):1127-34.

123. Hablitz LM, Pla V, Giannetto M, Vinitsky HS, Staeger FF, Metcalfe T, et al. Circadian control of brain glymphatic and lymphatic fluid flow. Nat Commun. 2020;11(1):4411.

국문초록

서론: 뇌척수액 림프 유출의 기능 장애와 그로 인한 뇌 노폐물 제거 감소는 노화 과정 및 신경 퇴행성 질환의 원인이 되는 것으로 밝혀지고 있음. 뇌척수액 림프 유출 기능 평가는 주로 형광 영상과 자기 공명 영상(MRI)에 의존했지만 이러한 방식은 생리 변화를 최소화하고 임상적용에 있어 제한이 있음. 본 연구는 마우스에서 뇌척수액 림프액 유출 평가를 위한 분자 영상 방법을 확립하고, 이를 활용하여 마우스 모델에서 연령에 따른 뇌척수액 림프 유출 기능 변화를 평가하고자 함.

방법: 분자 영상법 확립을 위해 우선 [^{99m}Tc]Tc-DTPA 와 [^{64}Cu]Cu-HSA 를 비교 평가하여 방사성 추적자를 선별함. 이후 대조(cisterna magna)와 척수강내(intrathecal) 주사 후 분포를 비교 평가하여 투여 경로를 선정함. 마지막으로 다양한 속도 및 부피 조건에서 추적자의 분포를 평가하여 최적의 투여 속도와 용량을 설정함. 최종 확립된 영상법을 15-25 개월 된 생쥐로 구성된 노화 마우스 모델에 적용하여 뇌척수액 림프 유출 기능을 정성적 및 정량적으로 평가함.

결과: [^{99m}Tc]Tc-DTPA 는 척수강내 주사 후 제거되는 과정에서 경부 림프절 섭취가 관찰되지 않음. [^{64}Cu]Cu-HSA 를 대조에 주사하였을 때 지속적인 주사부위 역류가 관찰되었으며 일관된 정량 평가에 제한이 있었음. Evans blue 및 [^{64}Cu]Cu-HSA 를 300 ~

500 nL/min 의 주입 속도(용량 3~9ul)로 투여하였을 때 추적자가 두개골 지주막하 공간에 도달하지 않았음. 종합하여, [^{64}Cu]Cu-HSA 를 척수강내에 700nL/min 의 주입 속도(용량 6ul)로 투여 후 전신 양전자 방출 단층촬영(PET) 영상을 시간대별로 획득하여 뇌척수액 림프 유출 기능을 평가함. 확립된 분자 영상법을 통해 성인(n=7) 및 노화(n=6) 마우스의 평균(± SD) 뇌척수액 제거 반감기는 93.4 ± 19.7 및123.3 ± 15.6 분($p = 0.01$) 이었음. 뇌척수액은 노화 마우스 모델에서 성인 마우스에 비해 전반적으로 더 느리게 제거되었으며 더 많이 잔류함.

결론**:** [^{64}Cu]Cu-HSA 를 활용하여 뇌척수액 림프 유출을 평가하기 위한 분자 영상 프로토콜을 확립하였으며 뇌척수액 림프 유출이 노화 마우스 모델에서 지연돼 있음을 확인함. 본 연구를 통해 확립한 분자 영상법은 전임상 뇌질환 모델에서 뇌척수액 림프 유출의 기능장애 평가를 위해 활용가능하며 향후 임상에서 뇌척수액 림프 유출 기능과 뇌질환 사이의 관계를 평가하는 도구로 활용이 기대됨.

주요어**:** 뇌척수액, 림프 유출, 수막 림프관, 노화, 양전자 방출 단층 촬영, 인간 혈청 알부민

학번**:** 2019-33343